PITX2 is a homeobox transcription factor that regulates left-right asymmetric morphogenesis[37,38] and it is also deeply implicated in myogenesis during mouse embryonic development[39–41]. We found that the decay of *Pitx2* mRNA is prolonged by knocking down MBNL1, but not CUGBP1 in undifferentiated C2C12 cells (Fig. 6b and c). This is consistent with the fact that *Pitx2* harbors a much higher number of MBNL1-CLIP tags than that of CUGBP1-CLIP tags in the 3′ UTR (Fig. 6a). We also observed that down regulation of both CUGBP1 and MBNL1 decreases the decay of *Myod1* and *Mbnl2* mRNA, but not that of *Gapdh* mRNA (Supplementary Fig. S8). Similarly, down regulation of CUGBP1 decreases the decay of other myogenic transcription factors such as *Myog* and *Mef2a* mRNAs, and also of *Cugbp2* (Supplementary Fig. S9). Furthermore, knockdown of CUGBP1 and MBNL1 prolongs decay of *Mbnl1* and *Cugbp1* mRNAs, respectively, suggesting a mechanism for cross-regulation of expression of MBNL1, CUGBP1, and their family proteins (Supplementary Fig. S8).

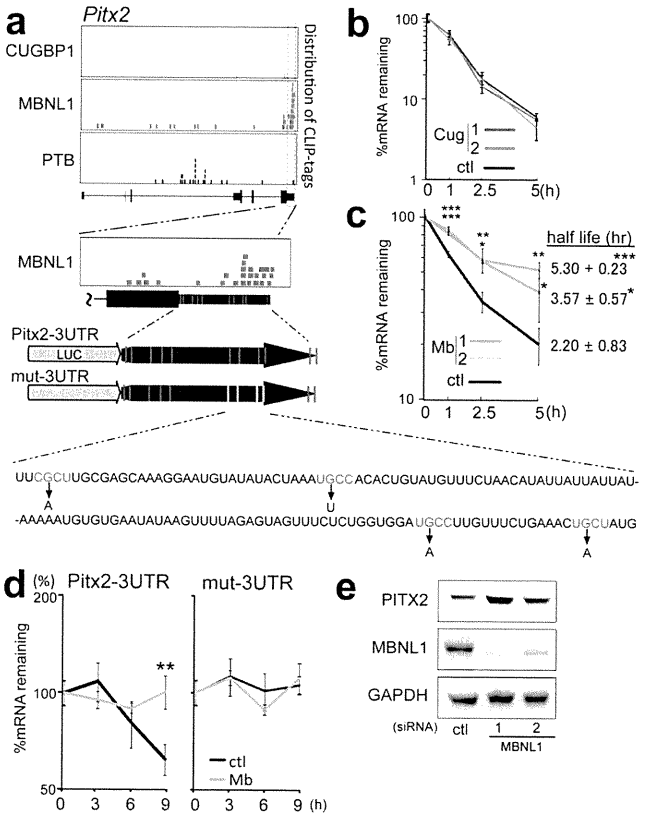

Figure 6 | MBNL1 binds to 3′ UTR of *Pitx2* and facilitates decay of *Pitx2* mRNA. (a) Distributions of MBNL1 CLIP-tags in the Pitx2-gene structure, and schemes of luciferase reporter plasmids harboring wild-type (Pitx2-3UTR) and mutated (mut-3UTR) 3′ UTRs of Pitx2. Red bars indicate locations of native YGCY motifs and yellow bars indicate those of mutated YGCY motifs. Individual mutations disrupting YGCY motifs are shown at the bottom. We introduced U at the 2nd YGCY motif to prevent formation of AU and AC repeats, which constitute a potential binding site of Hu proteins and hnRNP L, respectively. (b and c) Decay of endogenous Pitx2 mRNA by siRNA-mediated knockdown of CUGBP1 (b) and MBNL1 (c). C2C12 cells were treated with either control (ctl), CUGBP1 (Cug) or MBNL1 (Mb) siRNA. Actinomycin D was added to the medium to stop transcription at time 0. Temporal profiles of decay of the indicated genes were analyzed by real-time RT-PCR and were normalized for Gapdh mRNA levels. All experiments were triplicated, and the mean and s.d. are indicated (* $p < 0.05$; ** $p < 0.01$; *** $p < 0.001$). (d) Decay of luciferase mRNA in the Pitx2-3UTR and mut-3UTR constructs after either control (ctl) or MBNL1 (Mb) siRNA in TetON-C2C12 cells. Culture medium was replaced by medium without doxycycline to stop transcription at time 0. Temporal profiles of luciferase mRNA decay are quantified by real-time RT-PCR and are normalized for Gapdh mRNA levels. All experiments were triplicated, and the mean and s.d. are indicated (** $p < 0.01$). (e) Immunoblot of PITX2 in undifferentiated C2C12 cells at 48 hrs after transfection of MBNL1 siRNA.

To analyze more directly the role of MBNL1 binding to the 3′ UTR in regulation of mRNA decay, we examined the mRNA stability of firefly luciferase fused with the 3′ UTR of *Pitx2* (Fig. 6a). There are 11 YGCY motifs in the 3′ UTR of *Pitx2*, and 4 of the 11 motifs have MBNL1-CLIP tags. We introduced artificial mutations in these 4 motifs to prevent binding of MBNL1 (Fig. 6a). Consistent with the proposed role for MBNL1 in mRNA decay, we observe that disruption of the MBNL1-binding motifs in the *Pitx2*-3′ UTR abolished responsiveness to MBNL1 knockdown (Fig. 6d). Furthermore, immunoblots demonstrated that MBNL1-knockdown enhanced expression of endogenous PITX2 in C2C12 cells (Fig. 6e). These data suggest that MBNL1 promotes decay of *Pitx2* mRNA and thereby represses expression of the PITX2 protein.

Taken together, all of our data are consistent with a model where CUGBP1 and MBNL1 facilitate mRNA decay through binding to the 3′ UTR of target genes.

Discussion

CUGBP1 and MBNL1 are developmentally regulated RNA-binding proteins that are causally associated with myotonic dystrophy type 1. In this study, we show that both CUGBP1 and MBNL1 preferentially bind to 3′ UTRs and destabilize the bound mRNAs. In particular, we show that CUGBP1 and MBNL1 destabilize myogenic differentiation factors and RNA-binding proteins. In addition, our results confirm and significantly expand the current knowledge of the splicing-regulatory effects of CUGBP1 and MBNL1. Taken together, the data from the present study indicates that CUGBP1 and MBNL1 are closely related and cross regulate alternative splicing and mRNA decay.

MBNL1 binding to 3′ UTRs has not been previously reported. We show for the first time that MBNL1 binds to 3′ UTRs and promotes mRNA decay in both artificial constructs and in endogenous genes. We also demonstrate by expression arrays that both CUGBP1 and MBNL1 facilitate mRNA decay by binding to 3′ UTRs. The present study demonstrates global *in vivo* interactions between CUGBP1 and 3′ UTRs and reveals that CUGBP1 also preferentially binds to 3′ UTR rather than exons/introns. We provide *in vivo* evidence that CUGBP1 facilitates mRNA decay of a broad spectrum of genes in addition to the previously reported genes[25–27,42–44].

Interestingly, we find that MBNL1 promotes decay of *Cugbp1* mRNA and that CUGBP1 promotes decay of *Mbnl1* mRNA, and that this is associated with corresponding changes at the protein level during differentiation of C2C12 cells (Supplementary Fig. S4b). This may suggest that expression of CUGBP1 and MBNL1 are mutually regulated in myogenic differentiation. Kuyumcu-Martinez and colleagues report that expanded CUG repeats of *DMPK* through an unknown mechanism leads to phosphorylation and thereby to stabilization of CUGBP1 in DM1 myoblasts[10]. Our studies additionally suggest that loss of MBNL1 in DM1 could lead to decreased decay of *CUGBP1* mRNA and hence to further increase of CUGBP1 activity. Although CUGBP1 is not upregulated in adult MBNL1-knockout mice, this mechanism could lead to increased misregulation of splicing and decay of the mRNAs of target genes in embryonic development that culminates in the DM1 phenotype.

We find that binding sites for CUGBP1 and MBNL1 are enriched around alternative cassette exons (Fig. 2a). The binding sites for CUGBP1 are prominent in adjacent intronic regions flanking alternative exons. Our functional analysis reveals that binding of CUGBP1 to the upstream intron facilitates exon skipping, whereas

binding to the downstream intron enhances exon inclusion (Fig. 2b). Interestingly, similar regulation of alternative splicing has been observed for NOVA, FOX2 and PTB[30,45,46], indicating the presence of a common underlying mechanism shared by these proteins.

In contrast to CUGBP1, MBNL1 tags are also enriched in coding exons. Until now, splicing *cis*-elements of MBNL1 have been mapped exclusively to introns, and no exonic *cis*-element has been reported to our knowledge[20,23,34,47,48]. Although MBNL1 preferentially binds to exons, MBNL1 binding to introns is enriched at alternative rather than constitutive splice sites (Fig. 2a. This enrichment is diffusely distributed throughout regions harboring 500 nt upstream or downstream of alternative exons, in contrast to the prominent intronic peaks observed for CUGBP1 tags. This could suggest that MBNL1 needs to bind simultaneously to the target exon and adjacent introns to regulate splicing. Functional analysis of MBNL1 reveals that binding of MBNL1 close to the 3′ end of the downstream intron facilitates exon skipping, whereas no characteristic binding pattern is observed for exons included in response to MBNL1 (Fig. 2c). PTB has also been reported to regulate alternative splicing through binding close to the 3′ end of the downstream intron[36]. In contrast to MBNL1, however, binding of PTB to this region promotes exon inclusion. We similarly find binding of PTB to this region in our HITS-CLIP data in MBNL1-regulated exons (Supplementary Fig. S7d). Interestingly, the MBNL1-binding motif is enriched in PTB-regulated exons[46]. MBNL1 may thus compete for binding with other splicing factors like PTB and regulate alternative splicing events.

Post-transcriptional gene expression regulation is crucial to achieve precise developmental and tissue-specific control of cellular processes. Our studies reveal that CUGBP1 and MBNL1 preferentially bind to the 3′ UTRs of mRNAs encoding RNA-binding proteins and transcription factors, which can regulate cell development. During development of murine skeletal muscles, the nuclear level of MBNL1 increases, while that of CUGBP1 decreases[9,12]. Genes with mRNAs that can be bound both by CUGBP1 and MBNL1 are likely to be down-regulated by CUGBP1 in undifferentiated cells. If these genes need to be tightly down-regulated also in differentiated cells, MBNL1 can substitute for CUGBP1 in order to achieve continued destabilization of the target mRNA. We conclude that finely-tuned expression of CUGBP1 and MBNL1 may be important regulators of myogenic differentiation through precise regulation of both alternative splicing and mRNA stability.

Methods

Antibodies. Antibodies to CUGBP1 (3B1), MHC (H300), myogenin (M225) and PTB (N20) were purchased from Santa Cruz Biotechnology. Anti-GAPDH pAb was purchased from Sigma. Anti-PITX2 pAb was purchased from Abcam. Anti-MBNL1 rabbit serum (A2764) was a kind gift of Dr. Charles A. Thornton at University of Rochester. The specificity of antibodies against CUG BP1 and MBNL1 is supported by the data in previous reports 2,3 and also by our siRNA experiments (Supplementary Fig. S1).

Cell culture. Detailed methods are included in the Supplementary Information.

HITS-CLIP. C2C12 cells were UV-irradiated at 400 mJ and CLIP was performed as previously described[49]. High-throughput 36-bp single-end and 40-bp single-end sequencing was performed using an Illumina Genome Analyzer II. All HITS-CLIP data were registered in ArrayExpress with an accession number E-MTAB-414 and in ENA with an accession number ERP000789. Detailed information is provided in the Supplementary Information.

Bioinformatics analysis. Illumina reads were first prepared by removing the 4-bp tag and filtering sequences composed primarily of Illumina adapter. The resulting reads were mapped to the mouse genome (NCBI Build 37.1/mm9) with default parameters using the BWA[50] mapping software. To extract consensus motifs from the mapped reads, we considered only uniquely aligned reads and first removed duplicate reads to avoid potential PCR-mediated deviations in addition to bias from very highly expressed transcripts. We then extended the reads to 110 nt, the expected mean of the CLIP fragments and used the SeqMonk software (www.bioinformatics.bbsrc.ac.uk/projects/seqmonk) to identify binding regions by using the program's built-in peak detection algorithm. Peaks were scored using both a reads per peak scoring scheme and a maximum depth scoring scheme (effectively the height of the peak) in order to filter out peaks. For the identification of CUGBP1- and MBNL1-binding regions, we used PTB as a negative control and removed peaks present in the PTB dataset as well. We then selected CUGBP1 peaks that were present in the two independent CUGBP1 CLIP experiments and MBNL1 peaks that were similarly corroborated by the two MBNL1 experiments. PTB binding regions were identified by removing peaks that were present in either of the four CUGBP1 and MBNL1 experiments. Finally, we restricted the set of binding regions to only those spanning 70–150 bp since this was the fragment length used in the CLIP experiments. We analyzed each dataset using a motif analysis tool, MEME[51], using a background Markov model based on the entire mouse genome.

We analyzed the mapped Illumina reads and binding regions and mapped them to UCSC knownGene annotations[51] of the mouse genome (NCBI Build 37.1/mm9) by writing and running Perl and Excel VBA programs, as well as by running BEDTools utilities[52]. Normalized complexity maps of CUGBP1/MBNL1/PTB-RNA interactions were generated as previously described[30]. For the control, normalized complexity map was similarly generated by analyzing 100 sets of 15 to 50 constitutive exons that were randomly selected from 118,969 constitutive exons in mm9. To identify enriched Gene Ontology terms, we used the Database for Annotation, Visualization and Integrated Discovery (DAVID 6.7)[53,54].

Construction of plasmids. To construct luciferase reporter vectors with the 3′ UTR of *Gapdh* and *Pitx2*, 3′ UTRs of these genes were amplified by PCR. Amplified DNA was ligated into the *Xba*I and *Bam*HI sites of the pGL3-promoter vector (Promega) to substitute for the 3′ UTR of the firefly luciferase gene. DNA fragments harboring GT and CTG repeats were amplified by self-priming PCR using primers terminating in a *Xba*I site, and ligated into the *Xba*I site to make the pGL3P-*Gapdh*-3′ UTR.

To construct tet-responsive luciferase constructs, the tet-responsive promoter region was excised from pTRE-Tight vector (Clontech) with *Xho*I-*Hin*dIII site and cloned into the *Xho*I-*Hin*dIII site of the pGL3-promoter vector with the 3′ UTR of *Gapdh* and *Pitx2*. To introduce mutations in 3′ UTR of *Pitx2* in the luciferase construct, we used the QuikChange site-directed mutagenesis kit (Stratagene).

To construct expression vectors for MBNL1 and CUGBP1, the human MBNL1 cDNA and human CUGBP1 cDNA (Open Biosystems) were subcloned into the mammalian bidirectional expression vector pBI-CMV2 (Clontech), which should constitutively expresses the insert and AcGFP1.

RNA interference and transfection. The siRNA duplexes against CUGBP1 and MBNL1 were synthesized by Sigma. The sense sequences of the siRNAs were as follows: Cugbp1-1, 5′-GCUUUGGUUUUGUAAGUUA-3′; Cugbp1-2, 5′-GGCUUAAAGUGCAGCUCAA-3′; Mbnl1-1, 5′-CACUGGAAGUAUGUAGAGA-3′; and Mbnl1-2, 5′-GCACAAUGAUUGAUACCAA-3′. We purchased the AllStar Negative Control siRNA (1027281) from Qiagen. C2C12 cells were seeded on 24-well plates, and transfected with siRNA using Lipofectamine 2000 (Invitrogen) according to the manufacturer's instructions. Tet-off advanced HEK293 cells were seeded on 96-well plates, and were transfected with luciferase reporter gene constructs using FuGENE 6 (Roche) according to the manufacturer's instructions. At 48 hrs after transfection, cells were either harvested for RNA extraction or processed for isolation of total proteins or nuclear extracts.

RT-PCR for splicing analysis. Total RNA was extracted using Trizol (Invitrogen) according to the manufacturer's instructions. cDNA was synthesized using an oligo-dT primer and ReverTra Ace (Toyobo), and PCR amplifications were performed using GoTaq (Promega) for 30–35 cycles. Sequences of the primers used for PCR are listed in the Supplementary Table S3. The intensities of PCR-amplified spliced products were quantified with the ImageJ 1.42q software (NIH). We then calculated a percentage of exon inclusion (% inclusion) as the ratio of the intensity of the upper band divided by the sum of intensities of all the bands.

Real-time RT-PCR for RNA stability analysis. Total RNA was extracted using RNeasy mini kit (Qiagen) or CellAmp Direct RNA Prep Kit (Takara) according to the manufacturer's instructions. cDNA was synthesized as described above and real-time PCR was performed using the Mx3005P QPCR System (Stratagene) and the SYBR Premix Ex Taq II (Takara). Sequences of the primers used for PCR are listed in Supplementary Table S4.

Microarray analysis. Total RNA was extracted using the RNeasy mini kit according to the manufacturer's instructions. We synthesized and labeled cDNA fragments from 100 ng of total RNA using the GeneChip WT cDNA Synthesis Kit (Ambion). The labeled cDNAs were hybrized to the Affymetrix Mouse Exon 1.0 ST Arrays for splicing analysis or the Affymetrix Mouse Gene 1.0 ST Arrays for analyzing temporal profiles of expression of CUGBP1/MBNL1-targeted genes following the manufacturer's protocols. The robust multichip analysis (RMA) algorithm was used to normalize the array signals across chips with the Affymetrix Expression Console software 1.1.2. All microarray data were uploaded to the Gene Expression Omnibus database (accession numbers, GSE29990 for exon arrays and GSE27583 for expression arrays).

Western blotting. For preparation of total cell lysates, cells were lysed in buffer A (10 mM HEPES pH 7.8, 10 mM KCl, 0.1 mM EDTA, 1 mM DTT, 2 μg/ml Aprotinin, 0.5 mM PMSF, 0.1% NP-40) and incubate on ice for 20 min. After sonication, samples were centrifuged (15,000 rpm, 5 min) and the supernatants were stored at −80°C for further experiments. For preparation of nuclear cell lysates, cells were suspended in 400 μl of buffer A. Nuclei were pelleted, and the cytoplasmic

proteins were carefully removed. The nuclei were then resuspended in buffer C (50 mM HEPES pH 7.8, 420 mM KCl, 0.1 mM EDTA, 5 mM $MgCl_2$, 2% Glycerol, 1 mM DTT, 2 μg/ml Aprotinin, and 0.5 mM PMSF). After vortexing and stirring for 20 min at 4°C, the samples were centrifuged, and the supernatants were stored at −80°C. Samples were analyzed on a 10% SDS polyacrylamide gel, and the proteins were transferred to Immobilon polyvinylidene difluoride membranes (Millipore). Membranes were blocked with 1% BSA in Tris-buffered saline containing 0.05% Tween20 (TBST) for 1 hr, incubated for 1 hr with primary antibodies in TBST, washed three times with TBST, and incubated for 1 hr with horseradish peroxidase-conjugated anti-mouse or -rabbit immunoglobulin (GE) diluted 1 : 5,000 in TBST. After three washes in TBST, the blot was developed with the enhanced chemiluminescence system (GE) according to the manufacturer's instructions.

Luciferase assay. HEK293 cells seeded on a 96 well plate were transfected with 10 ng of pGL3P-*Gapdh*-3′ UTR with or without GT and CTG repeats, 5 ng of pRL/SV40 (Promega), and 40 ng of pBI-CMV2-based CUGBP1 or MBNL1 expression vector using FuGENE 6. At 48 hrs after the transfection, the luciferase activity was measured using the Dual-Luciferase Reporter Assay System (Promega) according to the manufacturer's instructions.

1. Licatalosi, D. D. & Darnell, R. B. RNA processing and its regulation: global insights into biological networks. *Nat Rev Genet* **11**, 75–87 (2010).
2. Wang, G. S. & Cooper, T. A. Splicing in disease: disruption of the splicing code and the decoding machinery. *Nat Rev Genet* **8**, 749–61 (2007).
3. Brook, J. D. *et al.* Molecular basis of myotonic dystrophy: expansion of a trinucleotide (CTG) repeat at the 3′ end of a transcript encoding a protein kinase family member. *Cell* **68**, 799–808 (1992).
4. Day, J. W. & Ranum, L. P. RNA pathogenesis of the myotonic dystrophies. *Neuromuscul Disord* **15**, 5–16 (2005).
5. Larkin, K. & Fardaei, M. Myotonic dystrophy—a multigene disorder. *Brain Res Bull* **56**, 389–95 (2001).
6. Lee, J. E. & Cooper, T. A. Pathogenic mechanisms of myotonic dystrophy. *Biochem Soc Trans* **37**, 1281–6 (2009).
7. Turner, C. & Hilton-Jones, D. The myotonic dystrophies: diagnosis and management. *J Neurol Neurosurg Psychiatry* **81**, 358–67 (2010).
8. Miller, J. W. *et al.* Recruitment of human muscleblind proteins to (CUG)(n) expansions associated with myotonic dystrophy. *EMBO J* **19**, 4439–48 (2000).
9. Lin, X. *et al.* Failure of MBNL1-dependent post-natal splicing transitions in myotonic dystrophy. *Hum Mol Genet* **15**, 2087–97 (2006).
10. Kuyumcu-Martinez, N. M., Wang, G. S. & Cooper, T. A. Increased steady-state levels of CUGBP1 in myotonic dystrophy 1 are due to PKC-mediated hyperphosphorylation. *Mol Cell* **28**, 68–78 (2007).
11. Iwahashi, C. K. *et al.* Protein composition of the intranuclear inclusions of FXTAS. *Brain* **129**, 256–71 (2006).
12. Kalsotra, A. *et al.* A postnatal switch of CELF and MBNL proteins reprograms alternative splicing in the developing heart. *Proc Natl Acad Sci U S A* **105**, 20333–8 (2008).
13. Bland, C. S. *et al.* Global regulation of alternative splicing during myogenic differentiation. *Nucleic Acids Res* (2010).
14. Philips, A. V., Timchenko, L. T. & Cooper, T. A. Disruption of splicing regulated by a CUG-binding protein in myotonic dystrophy. *Science* **280**, 737–41 (1998).
15. Ho, T. H., Bundman, D., Armstrong, D. L. & Cooper, T. A. Transgenic mice expressing CUG-BP1 reproduce splicing mis-regulation observed in myotonic dystrophy. *Hum Mol Genet* **14**, 1539–47 (2005).
16. Savkur, R. S., Philips, A. V. & Cooper, T. A. Aberrant regulation of insulin receptor alternative splicing is associated with insulin resistance in myotonic dystrophy. *Nat Genet* **29**, 40–7 (2001).
17. Charlet, B. N. *et al.* Loss of the muscle-specific chloride channel in type 1 myotonic dystrophy due to misregulated alternative splicing. *Mol Cell* **10**, 45–53 (2002).
18. Begemann, G. *et al.* muscleblind, a gene required for photoreceptor differentiation in Drosophila, encodes novel nuclear Cys3His-type zinc-finger-containing proteins. *Development* **124**, 4321–31 (1997).
19. Teplova, M. & Patel, D. J. Structural insights into RNA recognition by the alternative-splicing regulator muscleblind-like MBNL1. *Nat Struct Mol Biol* **15**, 1343–51 (2008).
20. Ho, T. H. *et al.* Muscleblind proteins regulate alternative splicing. *EMBO J* **23**, 3103–12 (2004).
21. Cass, D. *et al.* The four Zn fingers of MBNL1 provide a flexible platform for recognition of its RNA binding elements. *BMC Mol Biol* **12**, 20 (2011).
22. Kanadia, R. N. *et al.* A muscleblind knockout model for myotonic dystrophy. *Science* **302**, 1978–80 (2003).
23. Fugier, C. *et al.* Misregulated alternative splicing of BIN1 is associated with T tubule alterations and muscle weakness in myotonic dystrophy. *Nature Medicine* **17**, 720–5 (2011).
24. Moraes, K. C., Wilusz, C. J. & Wilusz, J. CUG-BP binds to RNA substrates and recruits PARN deadenylase. *Rna* **12**, 1084–91 (2006).
25. Vlasova, I. A. *et al.* Conserved GU-rich elements mediate mRNA decay by binding to CUG-binding protein 1. *Mol Cell* **29**, 263–70 (2008).
26. Lee, J. E., Lee, J. Y., Wilusz, J., Tian, B. & Wilusz, C. J. Systematic analysis of cis-elements in unstable mRNAs demonstrates that CUGBP1 is a key regulator of mRNA decay in muscle cells. *PLoS One* **5**, e11201 (2010).
27. Rattenbacher, B. *et al.* Analysis of CUGBP1 Targets Identifies GU-Repeat Sequences That Mediate Rapid mRNA Decay. *Mol Cell Biol* **30**, 3970–80 (2010).
28. Timchenko, N. A., Iakova, P., Cai, Z. J., Smith, J. R. & Timchenko, L. T. Molecular basis for impaired muscle differentiation in myotonic dystrophy. *Mol Cell Biol* **21**, 6927–38 (2001).
29. Timchenko, N. A. *et al.* Overexpression of CUG triplet repeat-binding protein, CUGBP1, in mice inhibits myogenesis. *J Biol Chem* **279**, 13129–39 (2004).
30. Licatalosi, D. D. *et al.* HITS-CLIP yields genome-wide insights into brain alternative RNA processing. *Nature* **456**, 464–9 (2008).
31. Bailey, T. L. & Elkan, C. The value of prior knowledge in discovering motifs with MEME. *Proc Int Conf Intell Syst Mol Biol* **3**, 21–9 (1995).
32. Marquis, J. *et al.* CUG-BP1/CELF1 requires UGU-rich sequences for high-affinity binding. *Biochem J* **400**, 291–301 (2006).
33. Du, H. *et al.* Aberrant alternative splicing and extracellular matrix gene expression in mouse models of myotonic dystrophy. *Nat Struct Mol Biol* **17**, 187–93 (2010).
34. Goers, E. S., Purcell, J., Voelker, R. B., Gates, D. P. & Berglund, J. A. MBNL1 binds GC motifs embedded in pyrimidines to regulate alternative splicing. *Nucleic Acids Res* (2010).
35. Kino, Y. *et al.* Muscleblind protein, MBNL1/EXP, binds specifically to CHHG repeats. *Hum Mol Genet* **13**, 495–507 (2004).
36. Xue, Y. *et al.* Genome-wide analysis of PTB-RNA interactions reveals a strategy used by the general splicing repressor to modulate exon inclusion or skipping. *Mol Cell* **36**, 996–1006 (2009).
37. Hamada, H., Meno, C., Watanabe, D. & Saijoh, Y. Establishment of vertebrate left-right asymmetry. *Nat Rev Genet* **3**, 103–13 (2002).
38. Yashiro, K., Shiratori, H. & Hamada, H. Haemodynamics determined by a genetic programme govern asymmetric development of the aortic arch. *Nature* **450**, 285–8 (2007).
39. Dong, F. *et al.* Pitx2 promotes development of splanchnic mesoderm-derived branchiomeric muscle. *Development* **133**, 4891–9 (2006).
40. Shih, H. P., Gross, M. K. & Kioussi, C. Cranial muscle defects of Pitx2 mutants result from specification defects in the first branchial arch. *Proceedings of the National Academy of Sciences of the United States of America* **104**, 5907–12 (2007).
41. Gherzi, R. *et al.* Akt2-mediated phosphorylation of Pitx2 controls Ccnd1 mRNA decay during muscle cell differentiation. *Cell Death and Differentiation* **17**, 975–83 (2010).
42. Chen, H. H., Xu, J., Safarpour, F. & Stewart, A. F. LMO4 mRNA stability is regulated by extracellular ATP in F11 cells. *Biochem Biophys Res Commun* **357**, 56–61 (2007).
43. Zhang, L., Lee, J. E., Wilusz, J. & Wilusz, C. J. The RNA-binding protein CUGBP1 regulates stability of tumor necrosis factor mRNA in muscle cells: implications for myotonic dystrophy. *J Biol Chem* **283**, 22457–63 (2008).
44. Horb, L. D. & Horb, M. E. BrunoL1 regulates endoderm proliferation through translational enhancement of cyclin A2 mRNA. *Dev Biol* (2010).
45. Yeo, G. W. *et al.* An RNA code for the FOX2 splicing regulator revealed by mapping RNA-protein interactions in stem cells. *Nat Struct Mol Biol* **16**, 130–7 (2009).
46. Llorian, M. *et al.* Position-dependent alternative splicing activity revealed by global profiling of alternative splicing events regulated by PTB. *Nat Struct Mol Biol* **17**, 1114–23 (2010).
47. Hino, S. *et al.* Molecular mechanisms responsible for aberrant splicing of SERCA1 in myotonic dystrophy type 1. *Hum Mol Genet* **16**, 2834–43 (2007).
48. Sen, S. *et al.* Muscleblind-like 1 (Mbnl1) promotes insulin receptor exon 11 inclusion via binding to a downstream evolutionarily conserved intronic enhancer. *J Biol Chem* **285**, 25426–37 (2010).
49. Ule, J., Jensen, K., Mele, A. & Darnell, R. B. CLIP: a method for identifying protein-RNA interaction sites in living cells. *Methods* **37**, 376–86 (2005).
50. Li, H. & Durbin, R. Fast and accurate long-read alignment with Burrows-Wheeler transform. *Bioinformatics* **26**, 589–95 (2010).
51. Rhead, B. *et al.* The UCSC Genome Browser database: update 2010. *Nucleic Acids Res* **38**, D613–9 (2010).
52. Quinlan, A. R. & Hall, I. M. BEDTools: a flexible suite of utilities for comparing genomic features. *Bioinformatics* **26**, 841–2 (2010).
53. Huang da, W., Sherman, B. T. & Lempicki, R. A. Systematic and integrative analysis of large gene lists using DAVID bioinformatics resources. *Nat Protoc* **4**, 44–57 (2009).
54. Dennis, G., Jr. *et al.* DAVID: Database for Annotation, Visualization, and Integrated Discovery. *Genome Biol* **4**, P3 (2003).

Acknowledgements

This work was supported by a JST-DASTI joint grant entitled "Strategic Japanese-Danish Cooperative Program on Molecular Medical Research", by Grants-in-Aid from the MEXT and MHLW of Japan, and by a grant from the Danish Medical Research Council (FSS Grant no. 271-07-342).

Author contributions

A.M., H.S.A, T.O., and M.I. performed the experiments. A.M., T.K.D., B.S.A., and K.O. analyzed the data. A.M., T.K.D., B.S.A. and K.O. prepared the manuscript. All authors reviewed the manuscript.

Additional information

Accession codes: All HITS-CLIP data were registered in ArrayExpress with an accession number E-MTAB-414 and in ENA with an accession number ERP000789.

All microarray data were uploaded to the Gene Expression Omnibus database with accession numbers, GSE29990 for exon arrays and GSE27583 for expression arrays.

Supplementary information accompanies this paper at http://www.nature.com/scientificreports

Competing financial interests: The authors declare no competing financial interests.

How to cite this article: Masuda, A. *et al.* CUGBP1 and MBNL1 preferentially bind to 3′ UTRs and facilitate mRNA decay. *Sci. Rep.* 1, 209; DOI:10.1038/srep00209 (2011).

ARTICLE IN PRESS

JNS-12138; No of Pages 5

Journal of the Neurological Sciences xxx (2012) xxx–xxx

Contents lists available at SciVerse ScienceDirect

Journal of the Neurological Sciences

journal homepage: www.elsevier.com/locate/jns

A novel mutation in SCN4A causes severe myotonia and school-age-onset paralytic episodes

Harumi Yoshinaga [a,*], Shunichi Sakoda [b], Jean-Marc Good [c], Masanori P. Takahashi [c], Tomoya Kubota [c], Eri Arikawa-Hirasawa [d], Tomohiko Nakata [e], Kinji Ohno [e], Tetsuro Kitamura [f], Katsuhiro Kobayashi [a], Yoko Ohtsuka [a]

[a] Department of Child Neurology, Okayama University Graduate School of Medicine, Dentistry, and Pharmaceutical Sciences, Okayama, Japan
[b] Department of Neurology, Kagoshima University Graduate School of Medical and Dental Sciences, Medical School, Kagoshima, Japan
[c] Department of Neurology, Osaka University Graduate School of Medicine, Osaka, Japan
[d] Department of Neurology, Juntendo University School of Medicine, Tokyo, Japan
[e] Division of Neurogenetics, Center for Neurological Diseases and Cancer, Nagoya University Graduate School of Medicine, Aichi, Japan
[f] Department of Pediatrics, Nipponkokan Fukuyama Hospital, Hiroshima, Japan

ARTICLE INFO

Article history:
Received 27 June 2011
Received in revised form 30 November 2011
Accepted 22 December 2011
Available online xxxx

Keywords:
Channelopathy
Na channel
Skeletal muscle
Activation
Slow inactivation
Schwarz–Jampel syndrome
SCN4A

ABSTRACT

Mutations in the pore-forming subunit of the skeletal muscle sodium channel (*SCN4A*) are responsible for hyperkalemic periodic paralysis, paramyotonia congenita and sodium channel myotonia. These disorders are classified based on their cardinal symptoms, myotonia and/or paralysis. We report the case of a Japanese boy with a novel mutation of *SCN4A*, p.I693L, who exhibited severe episodic myotonia from infancy and later onset mild paralytic attack. He started to have apneic episodes with generalized hypertonia at age of 11 months, then developed severe episodic myotonia since 2 years of age. He presented characteristic generalized features which resembled Schwarz–Jampel syndrome. After 7 years old, paralytic episodes occurred several times a year. The compound muscle action potential did not change during short and long exercise tests. Functional analysis of the mutant channel expressed in cultured cell revealed enhancement of the activation and disruption of the slow inactivation, which were consistent with myotonia and paralytic attack. The severe clinical features in his infancy may correspond to myotonia permanence, however, he subsequently experienced paralytic attacks. This case provides an example of the complexity and overlap of the clinical features of sodium channel myotonic disorders.

1. Introduction

To date, over 40 different mutations causing Na channelopathies of the skeletal muscle have been reported in *SCN4A* gene, which encodes for the pore-forming alpha-subunit of skeletal muscle sodium channel [1,2]. The Na channelopathies of the skeletal muscle are clinically classified into hyperkalemic periodic paralysis, paramyotonia congenita, or sodium channel myotonia on the basis of their clinical phenotype. However, phenotypic variability and marked overlap in symptoms have been reported [3–6]. The cases with severe phenotype in the neonatal period highlight the high clinical variability of sodium channelopathies [7,8]. The electrophysiological studies using heterologously expressed channels have shown that the missense mutations produces a gain-of-function defect of the fast gating such as disrupted fast inactivation and enhanced activation, which should result in increased excitability of the muscle membrane. It has been revealed that not only the defect of fast gating but also that of slow inactivation predisposes to paralytic attack, one of the clinical features of Na channelopathies [9,10].

In this report, we present a Japanese boy with skeletal dysplasia who exhibited very severe myotonia in infancy and mild paralytic attack after seven years of age. We identified a novel mutation in the intracellular loop linking segments 4–5 of domain II in *SCN4* and found that the heterologously expressed mutant channel showed enhancement of the activation and disruption of the slow inactivation.

2. Case report

2.1. Clinical features

The patient was delivered naturally and without complications. There is no family history of neuromuscular disease. Seven days after birth, he experienced transient breath-holding episodes with generalized muscle stiffness and facial pallor while crying. At 11 months of age, 30-second-long episodes of apnea arose with

* Corresponding author at: Shikatacho 2-5-1 Department of Child Neurology, Okayama University Graduate School of Medicine, Dentistry, and Pharmaceutical Sciences, Okayama 700–8558 Japan. Tel.: +81 86 235 7372; fax: +81 86 235 7377.
E-mail address: magenta@md.okayama-u.ac.jp (H. Yoshinaga).

0022-510X/$ – see front matter © 2012 Elsevier B.V. All rights reserved.
doi:10.1016/j.jns.2011.12.015

generalized hypertonia; these episodes were so severe that epileptic seizures were once suspected, but ictal EEG recordings did not indicate that this was the case. These episodes spontaneously disappeared, but at the age of two, the patient started to present daily fluctuating myotonia. The patient presented with a mask-like face with blepharospasm, grip myotonia, and dysarthria. These episodic myotonic attacks persisted for several minutes, hours, or even days, with fluctuation and created difficulties in standing, walking and upper-limb mobility. The symptoms seemed to be aggravated by cold (and were relieved during febrile illness) and fatigue, but not by potassium intake or exercise. The CK value fluctuated between 200 and 1000+ and tended to be high during myotonic attacks.

Fig. 1 depicts a generalized inter-episode feature when he was 5 years and 8 months old. Parental consent to present the photograph in Fig. 1 was obtained. He was of Herculean stature and exhibited several characteristic features, such as low-set ears, epicanthic folds, upturned nose, a long philtrum, puckered lips, short neck, hypertropic thighs, atrophic shoulder girdle muscles, pigeon breast, and joint contracture of the elbow. Accordingly, he was initially suspected as having a myogenic type of Schwarz–Jampel syndrome [4,11]. However, immunofluorescence stain for perlecan was normal in biopsied muscle and the histology revealed a nonspecific myopathic change with increased fiber variability. Acetazolamide, mexiletine, and phenytoin had some effect on his myotonic attacks. When these medications were discontinued on the day he underwent generalized anesthesia for the muscle biopsy, he experienced a very severe myotonic attack that involved the respiratory muscle.

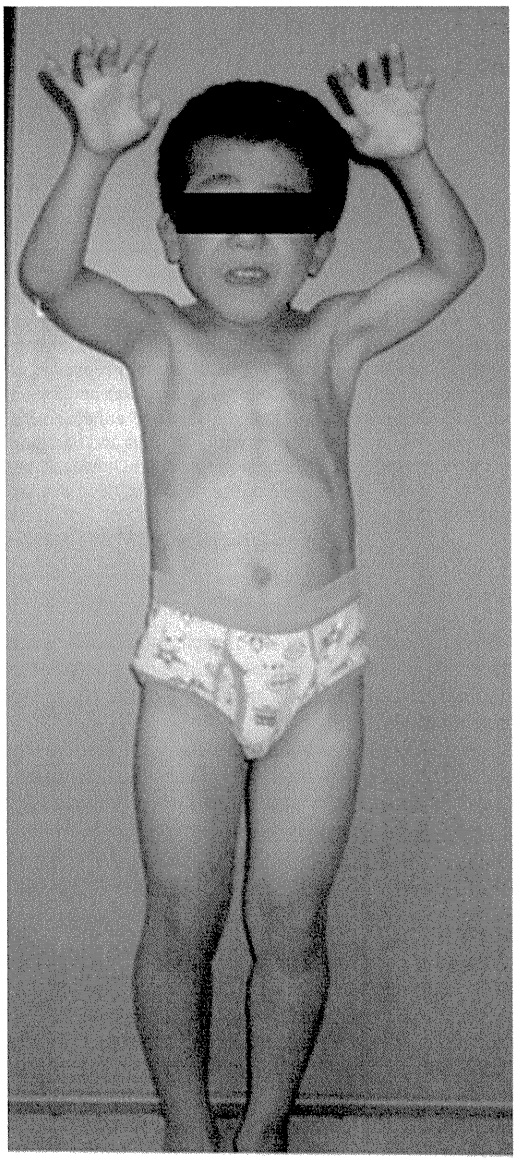

Fig. 1. The patient at 5 years and 8 months of age. Note his Herculean stature and hypertrophic thighs.

After 7 years and 8 months of age, paralytic episodes appeared that occurred several times a year thereafter, even in hot summertime temperatures. He complained of muscle weakness lasting from hours to several days at a time. His mother observed that his thighs become unusually soft during episodes. Neither exercise nor cooling brought about his episodic weakness.

2.2. Clinical electrophysiological analysis

Needle electromyography revealed diffuse continuous myotonic discharges accentuated by needle displacement with dive bomber sounds. Analysis of the compound muscle action potential (CMAP) amplitude before and after short or long exercise revealed no significant change [12]. Muscle cooling did not affect the CMAP either [13].

2.3. DNA analysis

Since there was no expansion of the repeat length at the DM1 locus with Southern blot, we analyzed the nucleotide sequence of *SCN4A* and *CLCN1* genes. Written informed consent was obtained from the parents for the mutation screening. This study was approved by the ethics committee of Kagoshima University Graduate School of Medical and Dental Sciences. Nucleotide sequence analysis of the patient's DNA showed a transition of A to C at the nucleotide in position 2077 (c.2077A>C) in *SCN4A* resulting in the substitution of isoleucine to leucine at amino acid in position 693 (p.I693L) (Fig. 2A). This mutation was not found in the DNA of the parents, both of whom were clinically non-affected. No mutations of *CLCN1* genes were identified by sequencing analysis.

Furthermore, the possibility of Schwarz–Jampel syndrome was excluded by re-sequencing all the exons and the flanking intronic regions of *HSPG2*. We enriched exonic fragments using the SureSelect Human All Exon v2 kit (Agilent, CA, USA), and read 50-bp fragments with the ABI SOLiD 4 sequencer (Applied Biosystems, CA, USA). We mapped 56,007,335 tags (89% of total tags) to human genome GRCh37.3/hg19 with BioScope 1.3.1 (Applied Biosystems), and read 2338 Mbp. Detection of SNVs with Avadis NGS (Strand Life Sciences, Bangalore, India) using default parameters revealed three homozygous missense SNPs that were all registered in dbSNP134 without any reference to clinical relevance (W71S, rs2254357, global minor allelic frequency (GMAF)=0.475; G242V, rs2254358, GMAF=0.476; and N765S, rs989994, GMAF=0.068).

2.4. Sodium channel functional study

We cultured human embryonic kidney (HEK) cells and transfected them with wild-type or mutant human sodium channel constructs as previously described [14]. Na+currents were recorded by the conventional whole-cell patch clamp technique. As shown in Fig. 3A, the mutant channels were consistently activated at more hyperpolarized voltages than the wild-type channels. To further investigate this phenomenon, the normalized sodium conductance at each measured peak current was calculated and plotted against the corresponding voltage. There was a marked shift towards hyperpolarized voltages in the activation curve of p.I693L mutant channels indicating an enhancement of the activation (Fig. 3B. Table 1).

Please cite this article as: Yoshinaga H, et al, A novel mutation in SCN4A causes severe myotonia and school-age-onset paralytic episodes, J Neurol Sci (2012), doi:10.1016/j.jns.2011.12.015

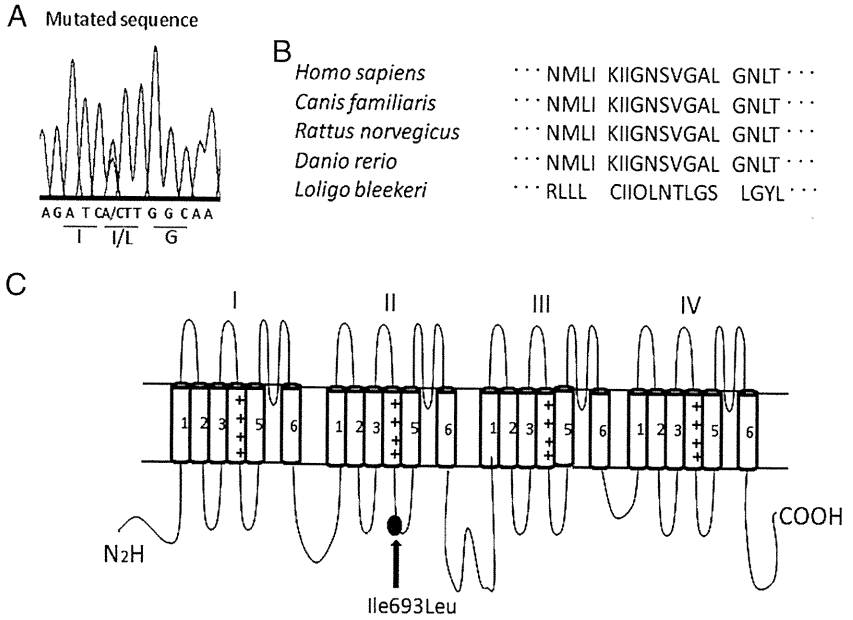

Fig. 2. A: DNA sequencing of the mutant region shows the transition of A to C at the nucleotide in position 2077 resulting in the substitution isoleucine (I) to leucine (L) at aminoacid in position 693 (I693L).B: Isoleucine residue in position 693 in Nav1.4 channel is preserved among homologs in many species.C: Schematic of the α subunit of Nav1.4 channel showing the six transmembrane segments (1–6) of each of the four domains (I–IV) and the location of p.I693L mutation (gray point).

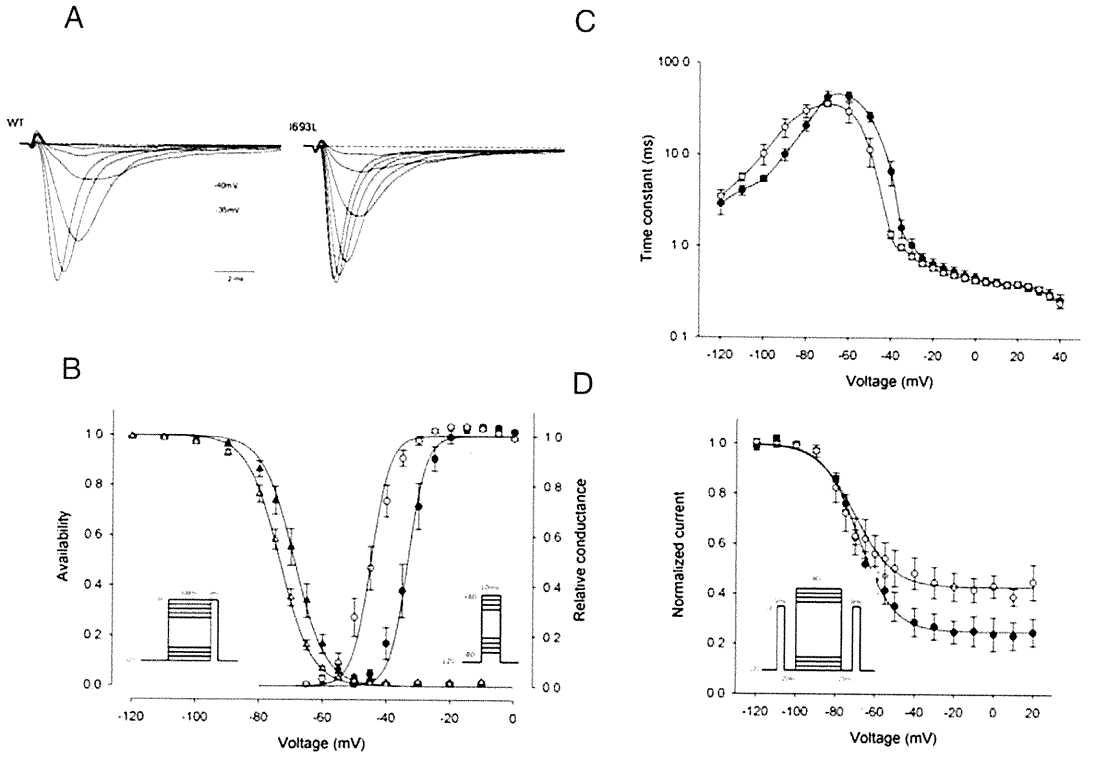

Fig. 3. A: Representative normalized currents recorded from HEK cells transfected with wild-type (WT) and I693L mutant channel and elicited by a series of 10 ms step pulse depolarizations from a holding potential of −120 mV to +40 mV in 5 mV increments. Activation is enhanced in I693L mutant channels.B: Activation (right-hand curves) for the wild-type ○ and I693L ● channels measured as the relative conductance of the peak sodium current elicited by depolarizing pulse from a holding potential of −120 mV to +40 mV (protocol in right inset). The activation voltage dependence of I693L mutant was shifted in the direction of hyperpolarization ($p<0.001$). Steady state fast inactivation (left-hand curves) for the wild-type △ and p.I693L ▲ channels measured as the relative peak current elicited by a −10 mV pulse after a 300 ms conditioning (protocol in left inset). We observed a shift towards negative voltages of the mutant constructs ($p=0.009$).C: Voltage dependence of the fast inactivation kinetics for the wild-type ○ and I693L ● channels measured by combining the data from three protocols (see results): a two-pulse recovery protocol (−120 mV to −80 mV), a two-pulse entry protocol (−70 mV to −40 mV) and a single-pulse relaxation protocol (−35 mV to +40 mV). The time constant for I693L channels was slightly slower at the negative voltages measured with the recovery protocol (n.s. $p>0.05$) and faster at the intermediate voltages measured with the entry protocol (from −50 mV to −35 mV $p<0.05$) than the wild-type. No difference was observed at more depolarized voltage.D: Peak sodium current elicited by a −10 mV test pulse was measured after a 60 s conditioning followed by a 20 ms gap at −120 mV to allow recovery from fast inactivation (protocol in the inset). The maximum extent of slow inactivation (1–I0) was smaller for I693L channels ●, revealing its impairment in comparison with the wild-type ○.

Please cite this article as: Yoshinaga H, et al, A novel mutation in SCN4A causes severe myotonia and school-age-onset paralytic episodes, J Neurol Sci (2012), doi:10.1016/j.jns.2011.12.015

Table 1
Gating parameter for WT and mutant Nav 1.4.

	Activation		Fast inactivation		Slow inactivation		
	V1/2(mV)	*k* (mV)	V1/2(mV)	*k* (mV)	V1/2(mV)	*k* (mV)	I0
WT	−33.3 ± 1.5 (9)	2.8 ± 0.4	−68.9 ± 1.6 (9)	5.0 ± 0.2	−68.3 ± 1.4 (5)	8.9 ± 1.1	0.25 ± 0.0522
p.I693L	−44.9 ± 1.5** (16)	2.9 ± 0.2	−73.5 ± 0.9* (5)	5.1 ± 0.2	−70.1 ± 3.3 (6)	9.6 ± 1.6	0.43 ± 0.0446*

Values are means + S.E.M, with number of experiments in parenthesis * significantly different from WT. $P<0.05$.
**significantly different from WT. $P<0.001$.

3. Discussion

Prior to identification of the sodium channel mutation, this patient was initially diagnosed as having a myogenic type of Schwartz–Jampel syndrome because of his characteristic appearance with severe myotonia [1,11]. The confusion between Schwartz–Jampel syndrome and sodium channelopathy was previously reported in a patient with myotonia permanence caused by G1306E mutation of SCN4A [4]. Our patient may also correspond to myotonia permanence, and he exhibited severe myotonic symptoms as apneic episodes from the neonatal period. Several patients with a *SCN4A* mutation, who showed severe symptoms including respiratory distress from an early neonatal period have also been reported [7,8]. One of these cases resembled Schwartz–Jampel syndrome [8].

Our patient showed severe myotonic episodes in his early infancy and then subsequent paralytic episodes. This case provides an example of the complexity and overlap of the clinical features of the sodium channel myotonic disorders, which sometimes make their classification difficult.

Some medications, including local anesthetics, anticonvulsants, and antiarrhythmics such as mexiletine, have shown efficacy for myotonic sodium channelopathies by blocking the sodium channel [2,15]. A carbonic anhydrase inhibitor, acetazolamide, is known to prevent paralytic attack but its antimyotonic action is in question. The myotonia of our patient showed a good response to mexiletine, phenytoin and acetazolamide, although carmabazepin showed little effect. Further studies are needed to understand the difference in efficacy between these drugs and the effects of acetazolamide.

The recently proposed standardized protocols involving short and long exercise tests in electromyographic analysis have improved the diagnosis of the subgroup of mutations in muscle channelopathies [12,13]. Fournier et al. [13] reported that combining the responses to several tests defined five electromyographic patterns that correspond to the subgroups of mutations. We applied their protocol to our patient and defined the response as pattern III [11] in which excitability is not impeded by any of the exercise trials. In their report [11], patients carrying G1306A or I693T (same locus on Nav 1.4 as ours [16]) sodium channel mutation also exhibited pattern III.

Functional analysis of the mutant channel revealed that the activation of the mutant channel was markedly enhanced in concordance with the enhanced excitability of our patient. However hyperpolarized shift of the steady-state inactivation curve which should reduce excitability, was also in a milder way observed in the mutant channel. The former may prevail over the latter, explaining the enhanced excitability which contributes to myotonia. Other mutations such as V445M [17], L689I [18], I704M, including the aforementioned I693T [16], have been found to similarly enhance both activation and fast inactivation and are often associated with myotonia.

Also, our data showed disrupted slow inactivation in the mutant construct, a defect which is expected to predispose to prolonged attack of paralysis. Our patient started to show episodic weakness recently. Again, I693T mutation showed an enhancement of activation with a slight shift towards hyperpolarized voltages for the steady state inactivation as well as a severely impaired slow inactivation [16]. The channel gating defects for I693T and its electromyographic pattern are strikingly similar with those observed for I693L. Unexpectedly, the I693T patient suffered from cold-induced weakness with a very mild myotonia [16]. The difference in hydrophobicity between the two mutated amino acids or the underlining genetic or environmental factors such as drug treatment can possibly modulate the expression of the disease.

Two other mutations, L689I and T70M, have been reported in the intracellular loop linking segments 4–5 of domain II in *SCN4A* [18]. Both have a phenotype of hyperkalemic periodic paralysis with a predominant weakness. The functional analysis of these mutant channels again revealed an enhancement of activation, and an impaired slow inactivation to a similar extent as for I693L mutant. These data and ours confirm the fact that the IIS4-S5 linker is one of the determinant regions for the sodium channel slow inactivation and to a various extent for the activation.

4. Conclusion

Further study of the genotype–phenotype correlations through individual cases will increase our knowledge of the variability of signs in this group of diseases and may also provide us with deeper insight into the function of the various regions of sodium channel proteins.

Acknowledgement

We thank Dr. Steve Cannon, University of Texas, for providing the expression vectors. This study was supported by Grants-in-Aids from the Ministry of Education, Culture, Sports, Science and Technology as well as the Ministry of Health, Labor and Welfare of Japan.

References

[1] Lehmann-Horn F, Rudel R, Jurkat-rott K. Nondystrophic myotonias and periodic paralyses. In: Engel AG, Franzini-Armstrong C, editors. Myology. 3rd ed. New York: McGraw Hill; 2004. p. 1257–300.
[2] Matthews E, Fialho D, Tan SV, Venamce SL, Cannon SC, Sternberg D, et al. The non-dystrophic myotonicas: molecular pathogenesis, diagnosis and treatment. Brain 2010;133:9–12.
[3] Plassart E, Eymard B, Maurs L, Hauw JJ, Lyon-Caen O, Fardeau M. Paramyotonia congenita: genotype to phenotype correlations in two families and report of a new mutation in the sodium channel gene. J Neurol Sci 1996;142:126–33.
[4] Colding-Jorgensen E, Duno M, Vissing J. Autosomal dominant monosymptomatic myotonia premanens. Neurology 2006;67:153–5.
[5] Lerche BH, Heine R, Pika U, George Jr AL, Mitovic N, Browatzki M, et al. Human sodium channel myotonia: slowed channel inactivation due to substitutions for a glycine within the III-IV linker. J Physiol 1993;470:13–22.
[6] Rudel R, Ricker K, Lehmann-Horn F. Genotype–phenotype correlations in human skeletal muscle sodium channel diseases. Arch Neurol 1993;50:1241–8.
[7] Lion-Francois L, Mignot C, Vicart S, Manel V, Sternberg D, Landrieu P, et al. Severe neonatal episodic laryngospasm due to de novo SCN4A mutation. Neurology 2010;75:641–5.
[8] Gay S, Dupuis D, Faovre L, Masurel-Paulet A, Labenne M, Colombani M, et al. Severe neonatal non-dystrophic myotonia secondary to a novel mutation of the voltage-gated sodium channel (SCN4A) gene. Am J Med Genet A 2008;146:380–3.
[9] Goldin AL. Mechanisms of sodium channel inactivation. Curr Opin Neurobiol 2003;13(3):284–90.
[10] Hayward LJ, Sandoval GM, Cannnon SC. Defective slow inactivation of sodium channels contributes to familial periodic paralysis. Neurology 1999;52:1447–53.

Please cite this article as: Yoshinaga H, et al, A novel mutation in SCN4A causes severe myotonia and school-age-onset paralytic episodes, J Neurol Sci (2012), doi:10.1016/j.jns.2011.12.015

[11] Topaloglu BH, Serdaroglu A, Okan M, Gucuyener K, Tope M. Improvement of myotonia with carbamazepine in three cases with the Schwartz–Jampel syndrome. Neuropediatrics 1993;24:232–4.
[12] Fournier E, Arzel M, Sternberg D, Vicart S, Laforet P, Eymard B, et al. Electromyography guides toward subgroups of mutations in muscle channelopathies. Ann Neurol 2004;56:650–61.
[13] Fournier E, Viala K, Gervais H, Sternberg D, Arzel M, Vicart S, et al. Cold extends electromyography distinction between ion channel mutations causing myotonia. Ann Neurol 2006;60:356–65.
[14] Hayward LJ, Brown Jr RH, Cannon SC. Inactivation defects caused by myotonia-associated mutations in the sodium channel III–IV linker. J Gen Physiol 1996;107:559–76.
[15] Heatwole CR, Moxley III RT. The nondystrophic myotonia. Neurotherapeutics 2007;4:238–51.
[16] Plassart-Schiess E, Lhuillier L, George Jr AL, Fontaine B, Tabti N. Functional expression of the Ile693Thr Na+ channel mutation associated with paramyotonia congenital in a human cell line. J Physiol 1998;507(3):721–7.
[17] Takahashi MP, Cannon SC. Enhanced slow inactivation by V 445M: a sodium channel mutation associated with myotonia. Biophys J 1999;76:861–8.
[18] Bendahhou S, Cummins TR, Kula RW, Fu YH, Ptacek LJ. Impairment of slow inactivation as a common mechanism for periodic paralysis in DIIS4-S5. Neurology 2002;58:1266–72.

Please cite this article as: Yoshinaga H, et al, A novel mutation in SCN4A causes severe myotonia and school-age-onset paralytic episodes, J Neurol Sci (2012), doi:10.1016/j.jns.2011.12.015

Nucleic Acids Research Advance Access published February 2, 2011

Nucleic Acids Research, 2011, 1–9
doi:10.1093/nar/gkr026

AG-dependent 3′-splice sites are predisposed to aberrant splicing due to a mutation at the first nucleotide of an exon

Yuan Fu, Akio Masuda, Mikako Ito, Jun Shinmi and Kinji Ohno*

Division of Neurogenetics, Center for Neurological Diseases and Cancer, Nagoya University Graduate School of Medicine, 65 Tsurumai, Showa-ku, Nagoya 466-8550, Japan

Received October 10, 2010; Revised December 23, 2010; Accepted January 12, 2011

ABSTRACT

In pre-mRNA splicing, a conserved AG/G at the 3′-splice site is recognized by U2AF^{35}. A disease-causing mutation abrogating the G nucleotide at the first position of an exon (E^{+1}) causes exon skipping in *GH1*, *FECH* and *EYA1*, but not in *LPL* or *HEXA*. Knockdown of U2AF^{35} enhanced exon skipping in *GH1* and *FECH*. RNA-EMSA revealed that wild-type *FECH* requires U2AF^{35} but wild-type *LPL* does not. A series of artificial mutations in the polypyrimidine tracts of *GH1*, *FECH*, *EYA1*, *LPL* and *HEXA* disclosed that a stretch of at least 10–15 pyrimidines is required to ensure normal splicing in the presence of a mutation at E^{+1}. Analysis of nine other disease-causing mutations at E^{+1} detected five splicing mutations. Our studies suggest that a mutation at the AG-dependent 3′-splice site that requires U2AF^{35} for spliceosome assembly causes exon skipping, whereas one at the AG-independent 3′-splice site that does not require U2AF^{35} gives rise to normal splicing. The AG-dependence of the 3′-splice site that we analyzed in disease-causing mutations at E^{+1} potentially helps identify yet unrecognized splicing mutations at E^{+1}.

INTRODUCTION

In higher eukaryotes, generation of functional mRNA is dependent on the removal of introns from pre-mRNA by splicing (1). The splicing process occurs in the spliceosome, the major components of which include five small nuclear RNAs and their associated proteins (U1, U2, U4, U5 and U6 snRNPs) in addition to a large number of non-snRNP proteins (2). In the first step of assembly of the spliceosome, U1 snRNP, SF1, U2AF^{65} and U2AF^{35} bind to the splicing *cis*-elements at the 5′ splice site (ss), the branch point sequence (BPS), the polypyrimidine tract (PPT) and the acceptor site, respectively, to form complex E (3).

Yeast has a well conserved BPS of UACUAAC (4), whereas we recently reported that human carries a highly degenerate BPS of yUnAy, where '*y*' and '*n*' represent pyrimidines and any nucleotides, respectively (5). Degeneracy of the human BPS supports a notion that the human BPS is likely to be recognized along with the downstream PPT where U2AF^{65} binds and possibly with the invariant AG dinucleotide at the 3′ ss where U2AF^{35} binds (6,7). U2AF^{65} and U2AF^{35} also make a heterodimer (8). In PPT, uridines are preferred over cytidines (9,10). In addition, PPT with 11 continuous uridines is highly competent and the position of such PPT is not critical (10). On the other hand, PPTs with only five or six uridines are required to be located close the 3′ AG for efficient splicing. In addition, phosphorylated DEK binds to and cooperates with U2AF^{35} for proper recognition of the 3′ ss (11).

In the next step of the spliceosome assembly, the bound U2AF^{65} and U2AF^{35} facilitate substitution of SF1 for U2snRNP at the branch point to form complex A. Introns carrying a long stretch of PPT do not require U2AF^{35} for this substitution, which is called 'AG-independent 3′ ss' (12–15). On the other hand, introns with a short or degenerate PPT require both U2AF^{65} and U2AF^{35} for this substitution, which is called 'AG-dependent 3′ ss'. Thereafter, the U4/U6.U5 tri-snRNP is integrated into the spliceosome to form complex B and the initial assembly of the spliceosome is completed.

The invariant AG dinucleotides are frequently reported targets of mutations causing human diseases, and the most frequent consequence is skipping of one or more exons (16). In addition, even mutations in highly degenerate BPS (5) and PPT (17) give rise to aberrant splicing

*To whom correspondence should be addressed. Tel: +81 52 744 2446; Fax: +81 52 744 2449; Email: ohnok@med.nagoya-u.ac.jp

causing genetic diseases (18). Disease-causing mutations also affect the first nucleotide of an exon (E^{+1}), but their effects on pre-mRNA splicing have been rarely scrutinized. As far as we know, only three such mutations in *FECH* (19), *GH1* (20) and *EYA1* (21) have been reported to cause aberrant splicing. Similarly, two such mutations in *LPL* (22) and *HEXA* (23) have been reported to have no effect on splicing. In this communication, we dissected molecular bases that differentiate splicing-disrupting and splicing-competent mutations, and found that AG-dependent ss is vulnerable to a mutation at E^{+1}, whereas AG-independent ss is tolerant.

MATERIALS AND METHODS

Minigene constructs and mutagenesis

Human genes of our interest were PCR-amplified from HEK293 cells using the KOD plus DNA polymerase (Toyobo). We introduced restriction enzyme-recognition sites at the 5′-end of the forward and reverse primers. We inserted the amplicon into the pcDNA3.1(+) mammalian expression vector (Invitrogen). We introduced patients' or artificial mutations with the QuikChange site-directed mutagenesis kit (Stratagene). We confirmed the absence of unexpected artifacts with the CEQ8000 genetic analyzer (Beckman Coulter).

Cell culture and transfection procedures

HEK293 cells were maintained in the Dulbecco's minimum essential medium (DMEM, Sigma-Aldrich) with 10% fetal bovine serum (FBS, Sigma-Aldrich). At ~50% confluency (~5×10^5 cells) in a 12-well plate, 1 ml of fresh Opti-MEM I (Invitrogen) was substituted for DMEM, and 500 ng of a minigene with 1.5 µl of the FuGENE6 transfection reagent (Roche Diagnostics) were then added. After 4 h, 2 ml of DMEM with 10% FBS was overlaid, and the cells were incubated overnight. The transfection medium was replaced with 2 ml of fresh DMEM with 10% FBS. RNA was extracted at 48 h after initiation of transfection.

RNA extraction and RT–PCR

Total RNA from HEK293 was extracted by Trizol reagent (Invitrogen) according to the manufacturer's protocols. The quantity and quality of RNA was determined by spectrophotometry (NanoDrop Techonologies). Twenty percent of the isolated RNA was used as a template for cDNA synthesis with the Oligo(dT) 12–18 Primer (Invitrogen) and the ReverTra Ace (Toyobo). Ten percent of the synthesized cDNA was used as a template for RT–PCR amplification with T7 primer (5′-TAATACG ACTCACTATAGGG-3′) and gene-specific primers for minigenes in pcDNA3.1(+). Image J software (National Institutes of Health) was used to quantify intensities of fragments. We employed JMP (SAS Institute) for statistical analysis.

RNA interference to knockdown $U2AF^{35}$

We synthesized siRNA of 5′-GGCUGUGAUUGACUU GAAUdTdT-3′ (GenBank accession number NM_006758, nucleotides 459–479), which is against the shared sequence of $U2AF^{35}$a and $U2AF^{35}$b (15). We employed Lipofectamine 2000 (Invitrogen) to cotransfect plasmids and siRNAs according to the manufacturer's protocols. Briefly, the transfection reagent included 300 ng of the plasmid, 50 pmol of siRNA, and 2 µl of lipofectamine 2000 in 100 µl of Opti-MEM I. The cells were harvested by western blotting for 48 h after transfection. The primary antibodies were goat polyclonal antibody for $U2AF^{35}$ (Santa Cruz Biotechnology), and mouse monoclonal antibodies for $U2AF^{65}$ (Santa Cruz Biotechnology) and PTB (Zymed Laboratories). The secondary antibodies were HRP-conjugated mouse anti-goat (Santa Cruz Biotechnology) or sheep anti-mouse (GE healthcare) antibodies. The immunoreactive proteins were detected by enhanced chemiluminescence (ECL, Amersham Biosciences).

For the siRNA rescue assay, we cloned the human $U2AF^{35}$ cDNA (Open Biosystems) into the HindIII and EcoRI restriction sites of the p3XFLAG-CMV-14 vector (Sigma-Aldrich). We introduced four silent mutations into the siRNA target region using the QuikChange site-directed mutagenesis kit with a primer, 5′-GAAAAG GCTGTAATCGATTTAAATAACCGTTGGTT-3′, where artificial mutations are underlined (24).

RNA probe synthesis

We synthesized [α-^{32}P]-CTP-labeled RNA using the Riboprobe *in vitro* transcription system (Promega) from a PCR-amplified fragment according to the manufacturer's instructions. We used the same forward primer for all the probes with the sequence of 5′-*TAATACGACTCACT ATAGG*GAGACAGG-3′, where the italicized is T7 promoter and the underlined is for annealing to the reverse primer. The four reverse primers were: wild-type *FECH*, 5′-TGGACCAACCTATGCGAAAGATAGACG AATGCGTAAGCCTGTCTC-3′; mutant *FECH*, 5′-TGG ACCAAACTATGCGAAAGATAGACGAATGCGTA AGCCTGTCTC-3′; wild-type *LPL*, 5′-TGGATCGAGG CCTTAAAAGGGAAAAAAGCAGGAACACCCTGT CTC-3′; and mutant *LPL*, 5′-TGGATCGAGGACTTAA AAGGGAAAAAAGCAGGAACACCCTGTCTC-3′, where the underlined is for annealing to the forward primer.

Expression and purification of recombinant proteins

The human $U2AF^{35}$ and $U2AF^{65}$ cDNAs were obtained from Open Biosystems. $U2AF^{35}$ and $U2AF^{65}$ cDNAs were subcloned into the *Bam*HI and *Eco*RI restriction sites of the pFastBac HTb vector. The recombinant baculoviruses were expressed using the Bac-to-Bac Baculovirus Expression System (Invitrogen) according to the manufacturer's instructions. Infected Sf9 cells were harvested after 48 h and resuspended in the lysis buffer containing 50 mM sodium phosphate, 10 mM imidazole, 300 mM NaCl, 1% Triton X-100, 2 mM

β-mercaptoethanol, the Complete Protease Inhibitor Cocktail (Roche Applied Science) and 5 U endonuclease in pH 7.0. His-tagged U2AF^{35} and U2AF^{65} proteins were purified using the TALON metal affinity resins (Clontech) under the denatured and native conditions, respectively. Purified U2AF^{35} was refolded by extended dialysis in dialysis buffer (50 mM sodium phosphate, 300 mM NaCl, 150 mM imidazole, pH 7.0). We determined the protein concentrations using the Pierce 660 nm Protein Assay Reagent (Thermo Scientific).

RNA-electrophoretic mobility shift assay

The radioactively labeled RNA (1×10^5 cpm) was incubated at room temperature with varying concentrations of recombinant proteins, 16 μg of yeast tRNA, and 1.6 U of RNasin (Toyobo) in a final volume of 20 μl of the binding buffer (20 mM HEPES pH 7.8, 50 mM KCl, 3 mM $MgCl_2$, 0.5 mM dithiothreitol, 0.5 mM EDTA and 5% glycerol). After 20 min, the RNA–protein complexes were separated on 5% non-denaturing polyacrylamide gels in 1 × TBE buffer at 4°C. The gels were dried and complex formation was visualized using the Typhoon 8600 Imager (GE Healthcare).

In silico analysis of the human genome and ESE-motifs

We analyzed human genome annotations (NCBI Build 37.1, hg19) by writing Perl programs, and executing them either on the PrimePower HPC2500/Solaris 9 supercomputer (Fujitsu) or on the cygwin UNIX emulator running on a Windows computer. To search for ESE-motifs, we used the ESE Finder (http://rulai.cshl.org/ESE/) (25,26), the RESUCE-ESE server (http://genes.mit.edu/burgelab/rescue-ese/) (27), the FAS-ESS server (http://genes.mit.edu/fas-ess/) (28), the PESX server (http://cubweb.biology.columbia.edu/pesx/) (29,30), and the ESRsearch server (http://ast.bioinfo.tau.ac.il/) (31).

RESULTS

Recapitulation of normal and aberrant splicing in minigenes

We first constructed minigenes of *GH1*, *FECH*, *EYA1*, *LPL* and *HEXA*, and introduced a previously reported disease-causing mutation at E^{+1} (Figure 1A). These minigenes successfully recapitulated normal and aberrant splicings: mutations in *GH1*, *FECH* and *EYA1* caused exon skipping, whereas those in *LPL* or *HEXA* did not (Figure 1B).

Down-regulation of U2AF^{35} increased exon skipping in wild-type *GH1* and *FECH*, but not in wild-type *EYA1*, *LPL* and *HEXA*

We predicted that a mutation at E^{+1} should disrupt binding of U2AF^{35}. We thus hypothesized that *GH1*, *FECH* and *EYA1* require binding of U2AF^{35} for the assembly of spliceosome, whereas *LPL* and *HEXA* do not require it. To prove this hypothesis, we first knocked down U2AF^{35} and analyzed its effect on the wild-type minigenes. We achieved an efficient down-regulation of U2AF^{35} in HEK293 cells (Figure 2A). We also confirmed

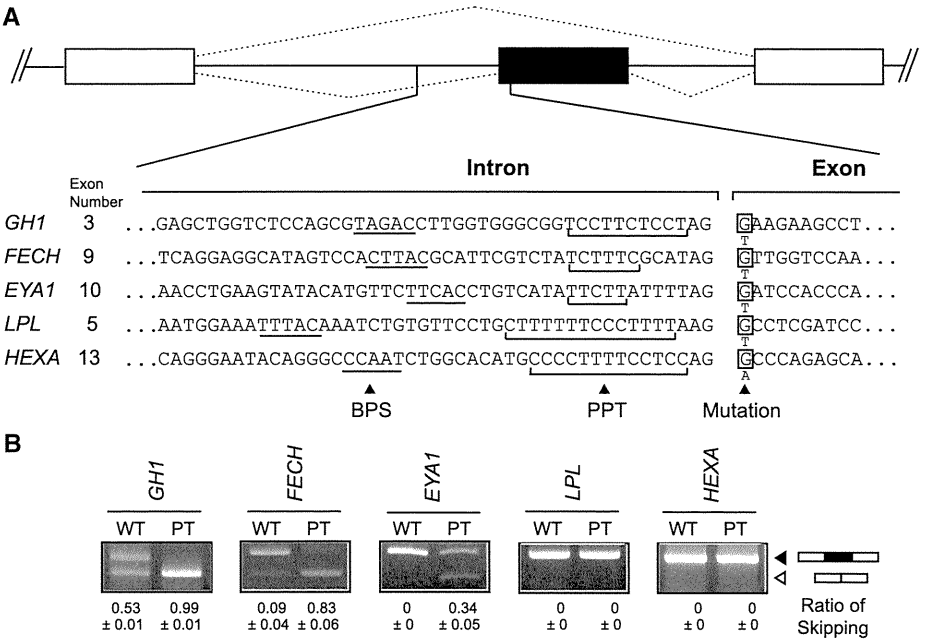

Figure 1. Recapitulation of normal and aberrant splicing of five genes. (**A**) Nucleotide sequences at the intron/exon junctions of five analyzed genes. Putative BPS is underlined. PPT is shown by a bracket. Mutant nucleotides are indicated at E^{+1}. (**B**) RT–PCR of minigenes expressed in HEK293 cells carrying the wild-type (WT) or patient's (PT) nucleotide. The mutations cause exon skipping in *GH1*, *FECH* and *EYA1*, but not in *LPL* and *HEXA*. Mean and SD of three independent experiments of the densitometric ratios of the exon-skipped product is shown at the bottom.

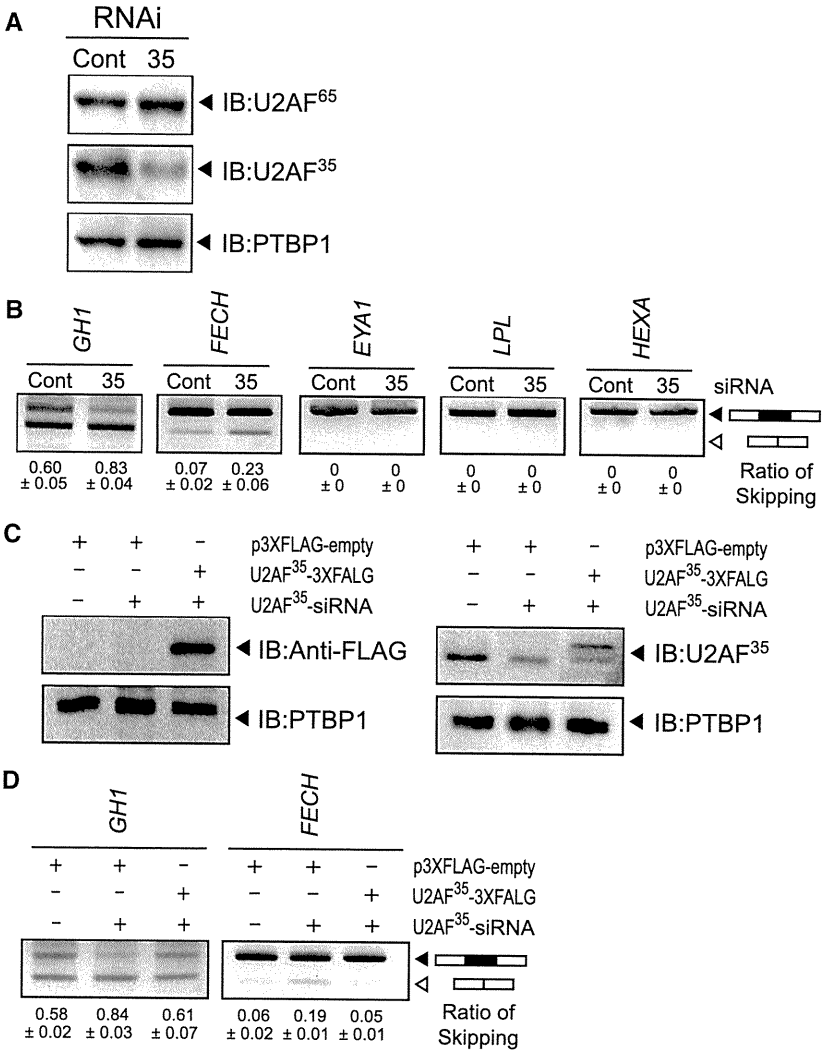

Figure 2. Effects of down-regulation of U2AF^{35} on pre-mRNA splicing. (**A**) Western blots demonstrating that U2AF^{35}-siRNA efficiently knocks down U2AF^{35} but not U2AF^{65} or PTBP1. (**B**) Down-regulation of U2AF^{35} facilitates exon skipping in wild-type *GH1* and *FECH*, but not in wild-type *EYA1*, *LPL* and *HEXA*. (**C**) Introduction of an siRNA-resistant p3XFLAG-U2AF^{35} encoding 3× FLAG fused with U2AF^{35} is visualized by immunoblots against FLAG and U2AF^{35}. (**D**) Exon skipping facilitated by U2AF^{35}-siRNA is partially rescued by introduction of the siRNA-resistant p3XFLAG-U2AF^{35}.

that the U2AF^{35}-siRNA had no effect on the expression level of U2AF^{65}. As expected, the down-regulation of U2AF^{35} increased exon skipping of *GH1* and *FECH* (Figure 2B) but not to the levels of the mutant constructs (Figure 1B). Again, as expected, we observed no effect on *LPL* and *HEXA*. Unexpectedly, however, *EYA1* demonstrated no response to the down-regulation of U2AF^{35}. Less efficient effects of U2AF^{35}-siRNA on *GH1*, *FECH* and *EYA1* (Figure 2B) compared to the mutant constructs (Figure 1B) were likely because the mutation abolished binding of U2AF^{35} in all the cells, whereas substantial numbers of cells failed to incorporate U2AF^{35}-siRNA and gave rise to normally spliced products.

We additionally introduced the siRNA-resistant p3XFLAG-U2AF^{35} to ensure that the effect of siRNA-U2AF^{35} was not due to off-target effects (Figure 2C). As expected, coexpression of p3XFLAG-U2AF^{35} partially rescued the splicing defects in *GH1* and *FECH* (Figure 2D).

U2AF^{35} is required for binding of U2AF^{65} to PPT in *FECH* but not in *LPL*

To further prove that U2AF^{35} is required for pre-mRNA splicing, we employed an electrophoretic mobility shift assay (EMSA) using wild-type and mutant RNA substrates of *FECH* and *LPL* (Figure 3A). His-tagged U2AF^{35} and U2AF^{65} were expressed using bacluovirus and were purified under denatured and native conditions, respectively. Denatured U2AF^{35} was refolded before RNA-EMSA. As expected, U2AF^{65} failed to bind to the wild-type *FECH* in the absence of U2AF^{35}, and addition

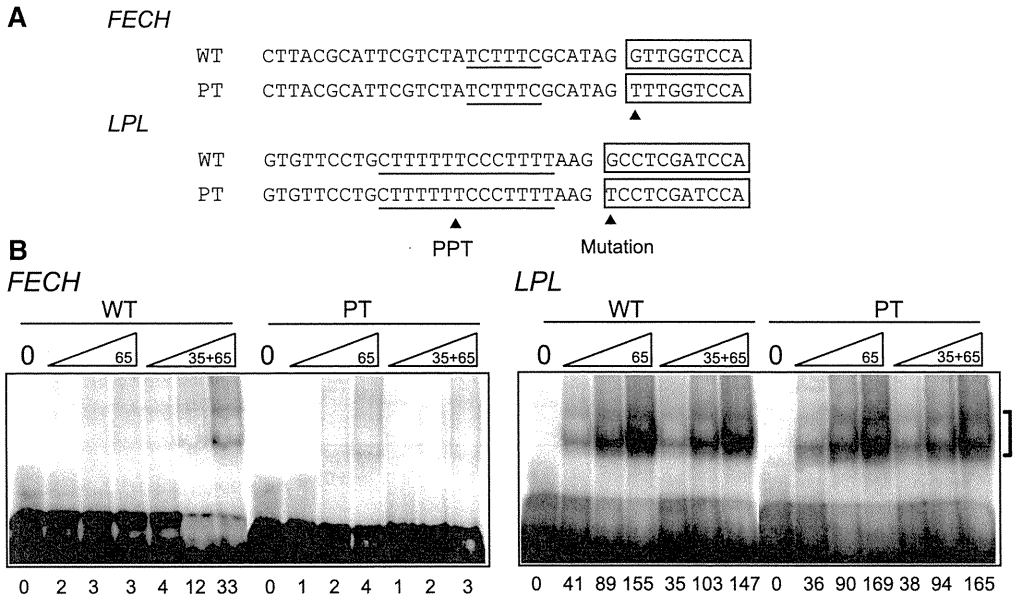

Figure 3. RNA-EMSA. (**A**) Sequences of wild-type (WT) and mutant (PT) RNA probes of *FECH* and *LPL* employed for RNA-EMSA. (**B**) RNA-EMSA of wild-type and mutant *FECH* and *LPL* with increasing amounts of $U2AF^{65}$ with or without $U2AF^{35}$. His-tagged $U2AF^{65}$ and $U2AF^{35}$ are expressed in Sf9 cells and are purified. Wild-type *FECH* requires $U2AF^{35}$ to bind to $U2AF^{65}$, whereas wild-type *LPL* does not require $U2AF^{35}$. A mutation at E^{+1} abrogates binding of $U2AF^{65}$ in *FECH* but not in *LPL*. Concentrations of $U2AF^{35}$ are 5, 10 and 20 ng/μl; and those of $U2AF^{65}$ are 10, 20 and 40 ng/μl. Numbers at the bottom indicate intensities of the retarded fragments in arbitrary units.

of $U2AF^{35}$ gained its binding. For the mutant *FECH*, neither $U2AF^{65}$ alone nor addition of both U2AFs showed binding of U2AFs. On the other hand, the wild-type *LPL* did not require $U2AF^{35}$ to bind to $U2AF^{65}$. Addition of $U2AF^{35}$ did not substantially increased binding of $U2AF^{65}$. These bindings were not affected by the mutation at E^{+1} of *LPL* (Figure 3B).

These results indicate that the mutation in *FECH* compromises a binding affinity for $U2AF^{35}$, which in turn abrogates binding of $U2AF^{65}$ and results in aberrant splicing. On the other hand, wild-type *LPL* does not need to bind to $U2AF^{35}$ and the mutation at E^{+1} has no effect on the assembly of spliceosome.

PPT determines the splicing consequences of the mutations

In an effort to delineate effects of the PPT sequences on the splicing consequence of a mutation at E^{+1}, we introduced a series of mutations into the PPT in the presence of the mutation at E^{+1}. Extensions of the polypyrimidine stretch ameliorated aberrant splicing in *GH1*, *FECH* and *EYA1*. Conversely, truncations or disruptions of the polypyrimidine stretch caused exon skipping in *LPL* and *HEXA* (Figure 4).

Length of the polypyrimidine stretch best predicts the splicing consequences

We next sought for parameters that differentiate normal and aberrant splicings in these minigenes. Analysis of parameters that potentially dictate the strength of the PPT indicated that the length of pyrimidine stretch, the number of pyrimidines in 25 or 50 nt at the 3′-end of an intron correlated with the ratio of exon skipping with correlation coefficients of more than 0.6 (Supplementary Table S1). The number of pyrimidines in 25 or 50 nt at the 3′-end of an intron, however, failed to predict splicing consequences of nine other constructs shown in Figure 6, and is likely to be overfitted parameters unique to the 35 constructs in Figure 4. Coolidge and colleagues report that $(GU)_{11}$ in PPT is partly functional, but we did not observe alternative purine and pyrimidine residues in our PPTs and did not quantify effects of alternative nucleotides (10). We thus took the length of pyrimidine stretch as a best parameter to dictate the strength of the PPT (Figure 5A). The native *GH1*, *FECH* and *EYA1* carry a stretch of 6–10 pyrimidines, whereas the native *LPL* and *HEXA* harbor a stretch of 14 and 13 pyrimidines, respectively (arrows in Figure 5A). For highly degenerate PPTs in the artificial constructs, the total number of pyrimidines in a stretch of 25 nt at the 3′-end of an intron well predicts the ratio of exon skipping (Figure 5B). These analyses revealed that the length of the polypyrimidine stretch should be at least 10–15 nt to ensure normal splicing even in the presence of a mutation at E^{+1}.

Identification of effects on pre-mRNA splicing of nine disease-associated mutations at the first nucleotide of an exon

We next examined other mutations at E^{+1} in which splicing consequences have not been previously analyzed. We first identified 224 mutations that abrogate the first 'G' nucleotide of an exon in the Human Gene Mutation Database at http://www.hgmd.cf.ac.uk/ (data not shown). Among these, we arbitrarily chose nine mutations causing

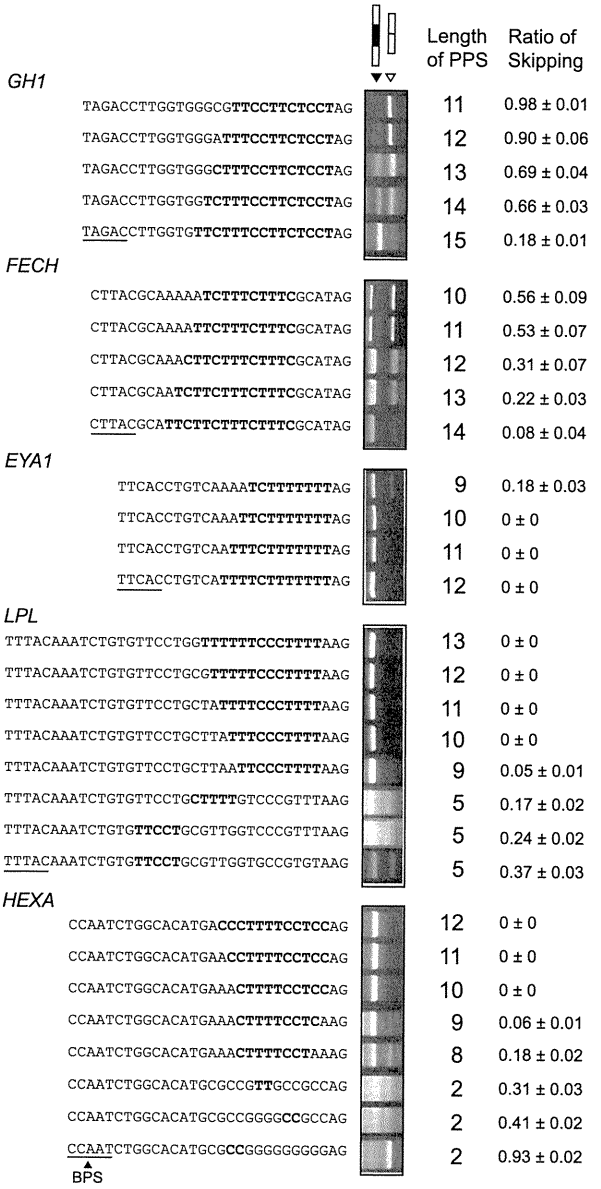

Figure 4. RT–PCR of HEK293 cells transfected with minigenes carrying artificially extended or disrupted PPT's. All the constructs harbor a mutation at E^{+1}. The top construct of each gene represents the patient's sequence. Only the nucleotide sequences of the 3′-end of an intron are indicated. The longest stretches of the polypyrimidines are shown in bold. Underlines indicate putative BPS's. The rightmost column shows the mean and SD of three independent experiments of the densitometric ratios of the exon-skipped product.

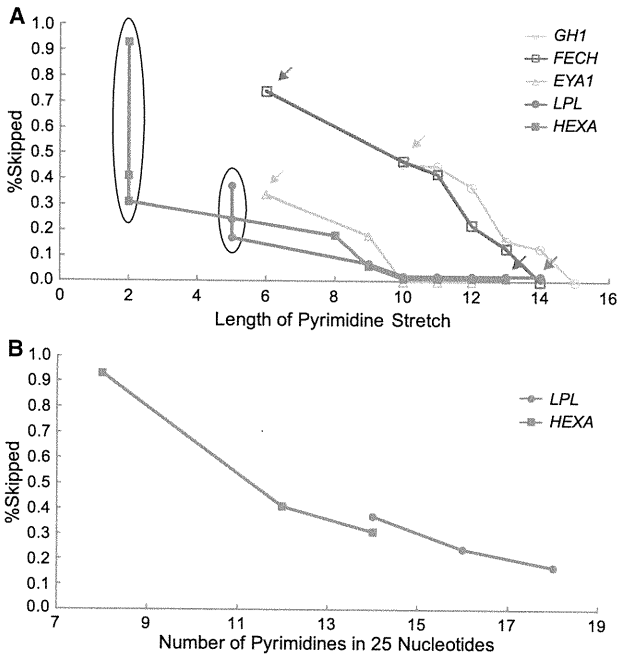

Figure 5. Ratios of exon skipping are plotted against the lengths of the polypyrimidine stretch (**A**) and the numbers of pyrimidines in 25 nt at the 3′-end of an intron (**B**). The ordinate (percent skipped) represents the ratios of exon skipping compared to that of the wild-type construct. The data are obtained from RT–PCR shown in Figure 4. Arrows indicate the original constructs carrying the patient's sequence, and the others are artificial constructs. Six constructs indicated by ovals in (A) are plotted in (B).

neuromuscular and musculoskeletal disorders (Figure 6A).

We constructed nine pairs of wild-type and mutant minigenes, and introduced them into HEK293 cells. We observed aberrant splicing in *PKHD1*, *COL1A2* (exon 37), *CLCN2*, *CAPN3* (exons 10 and 17), but not in *LAMA2*, *NEU1*, *COL6A2* and *COL1A2* (exon 23) (Figure 6B). The lengths of the polypyrimidine stretch of the five aberrantly spliced constructs ranged from 4 to 10 nt, whereas those of the four normally spliced constructs ranged from 9 to 16 nt. These results are in concordance with a notion that the short polypyrimidine stretches are predisposed to aberrant splicing due to a mutation at E^{+1}, whereas long polypyrimidine stretches are tolerant to such mutations. Among the 224 mutations affecting 'G' at E^{+1}, only three mutations have been reported to cause aberrant splicing. We here analyzed nine mutations and identified five more such mutations. It is thus likely that most splicing mutations at E^{+1} still remain unrecognized to date.

Analysis of the 3′-splice sites of the human genome

We next analyzed PPTs of 176 809 introns of the entire human genome. The length of the pyrimidine stretch was shorter when E^{+1} was the conserved 'G' (Figure 7A). This also supports a notion that AG-dependent 3′ ss harboring G at E^{+1} has a short polypyrimidine stretch (12). In addition, the ratio of 'C' at intronic position −3 was lower when E^{+1} was the conserved 'G' (Figure 7B), which suggests that G at E^{+1} makes C at −3 dispensable for binding to U2AF[35], although this is not directly relevant to the length of the PPT.

Being prompted by a previous report that U2AF[35] binds up to the 10th nucleotide of an exon (12), we examined nucleotide frequencies at exonic positions +1

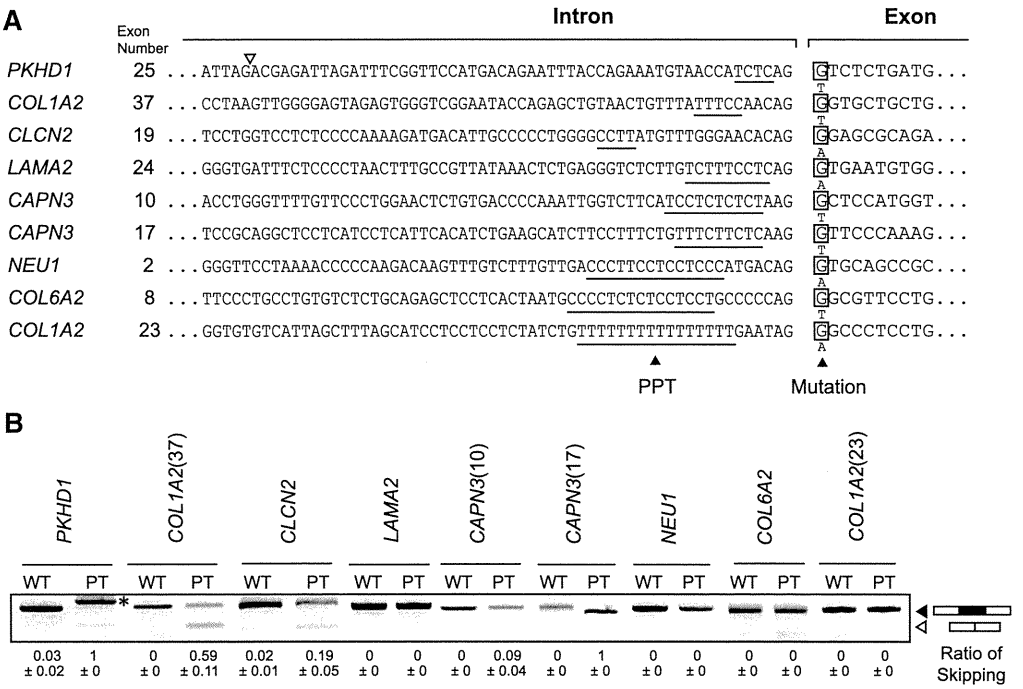

Figure 6. RT–PCR analysis of nine disease-causing mutations at E^{+1}. (**A**) Sequences at the intron/exon junctions of nine pairs of wild-type and mutant constructs. The longest polypyrimidine stretches are underlined. (**B**) RT–PCR of minigenes transfected into HEK293 cells. Five mutant constructs are aberrantly spliced, whereas the remaining four mutants are normally spliced. Numbers in the parentheses indicate exon numbers. In *PKHD1*, a cryptic 3′-splice site (open arrowhead in panel A) at 55 nt upstream of the native site is activated (asterisk). Mean and SD of three independent experiments of the densitometric ratios of the exon-skipped product is shown at the bottom.

to +12. We counted only wobbling nucleotides based on the human genome annotation NCBI Build 37.1 (hg19). As expected, 'GT' dinucleotide was frequently observed at exonic positions +1 and +2. We also observed preference for a 'T' nucleotide at positions +3 to +5 (Figure 7C). Alignment of SELEX results of $U2AF^{35}$ by Wu and colleagues (12) similarly demonstrate overrepresentation of 'T' nucleotides at positions +3 to +6 (Figure 7D). We thus analyzed effects of 'TTT' at positions +3 to +5 using the *GH1, FECH* and *EYA1* minigenes carrying the patient's mutations. We found that introduction of 'TTT' at exonic position +3 to +5 had no effect in *GH1* and *FECH*, but slightly enhanced exon recognition in *EYA1* (Figure 7E).

DISCUSSION

We previously reported that the SD-score algorithm efficiently predicts splicing consequences of a mutation affecting the 5′ ss (32). We next identified that the human BPS consensus is simply yUnAy (5), and hoped to predict if a given mutation affecting the BPS causes aberrant splicing or not. The high degeneracy of the BPS consensus, however, prevented us from constructing an efficient algorithm. In this communication, we worked on mutations at E^{+1}. As far as we know, only three such mutations have been reported to cause aberrant splicing, and only two such mutations have been reported not to affect splicing. Knockdown and RNA-EMSA of $U2AF^{35}$, as well as analyses of artificial PPT mutations and nine disease-causing mutations at E^{+1} revealed that AG-dependence of 3′ ss determines the splicing consequences. In the presence of a mutation at E^{+1}, a stretch of 15 or more pyrimidines ensures normal splicing, whereas a stretch of 10 or less pyrimidines are predisposed to aberrant splicing.

AG-dependent 3′ ss requires both $U2AF^{65}$ and $U2AF^{35}$ to bring U2snRNP to the branch point, whereas AG-independent 3′ ss has a long stretch of pyrimidines that can bind to $U2AF^{65}$ without $U2AF^{35}$ (13,15). $U2AF^{35}$ potentially provides an additional RNA–protein interacting force and an additional SR protein-binding surfaces (33). An artificial G-to-C mutation at E^{+1} downstream of a stretch of five pyrimidines in the mouse IgM gene abrogates binding of $U2AF^{35}$ and causes defective splicing (14). Similarly, in *INSR* exon 11 carrying an 'A' nucleotide at E^{+1}, a stretch of 14 pyrimidines but not of 10 pyrimidines is properly spliced (34). Additionally, a stretch of eight pyrimidines upstream of the last exon with 'C' at E^{+1} of *EIF3S7* is dependent on $U2AF^{35}$, whereas a stretch of 14 pyrimidines upstream of the last exon with 'A' at E^{+1} of *CUEDC1* is independent (15). Our observations and previous reports all point to a notion that effects on pre-mRNA splicing should be scrutinized for a mutation at E^{+1} if the preceding intron carries a short stretch of 10 or less pyrimidines. Indeed, in our analysis of nine disease-causing mutations, five of six mutants with 10 or less contiguous pyrimidines were aberrantly spliced (Figure 6), but no splicing analysis has been documented for any of them.

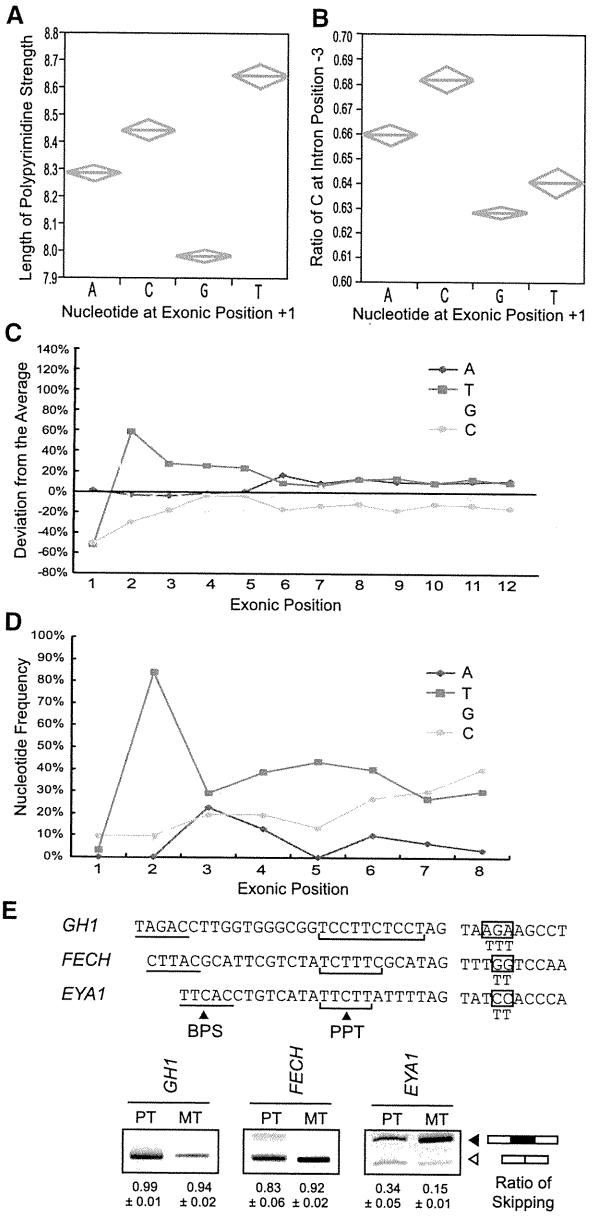

Figure 7. (**A**) Polypyrimidine stretch and the first nucleotide of an exon in the human genome. The longest stretch of uninterrupted pyrimidines among 25 nt at the 3′-ends of an intron is counted for 176 809 introns of the human genome. Diamonds represent means and 95% confidence intervals. One-way ANOVA and Fisher's-multiple range test revealed statistical significance of $P < 0.0001$. (**B**) Ratios of 'C' at position −3 in relation to the first nucleotide of an exon are analyzed for 176 809 introns of the human genome. Diamonds represent means and 95% confidence intervals. One-way ANOVA and Fisher's-multiple range test revealed statistical significance of $P < 0.0001$. (**C**) Preferentially observed nucleotides at the 5′-end of an exon in human. Only wobbling nucleotides are counted in the human genome. (**D**) Nucleotide frequencies at exonic positions +1 to +8 according to the SELEX data of U2AF^{35} by Wu and colleagues (12). (**E**) Effects of 'TTT' at exonic positions +3 to +5 in *GH1*, *FECH* and *EYA1* carrying the patient's mutation at E^{+1}. Artificially substituted exonic nucleotides are indicated by boxes. Mean and SD of three independent experiments of the densitometric ratios of the exon-skipped product is shown at the bottom.

We first report overrepresentation of 'T' nucleotides at exonic positions +3 to +5 in the human genome, as well as in *in vitro* U2AF^{35}-binding sites. Enhancement of exon recognition in *EYA1* by introduction of 'TTT' at positions +3 to +5 also underscores a notion that 'TTT' at +3 to +5 is likely to enhance binding of U2AF^{35}. Effects of 'TTT', however, were not observed in *GH1* and *FECH*. As the patient's mutation in *GH1* and *FECH* resulted in almost complete skipping of an exon, whereas that in *EYA1* gave rise to both exon-skipped and included products. The degrees of aberration of exon recognition may account for the 'TTT'-responsiveness. Alternatively, although no ESE motif was detected in the 'TTT'-introduced *EYA1* by five different ESE search tools, an unrecognized ESE might have ameliorated exon skipping in *EYA1*. Further analysis is required to elucidate effects of overrepresentation of 'T' at positions +3 to +5.

SUPPLEMENTARY DATA

Supplementary Data are available at NAR Online.

FUNDING

Grants-in-Aids from the Ministry of Education, Culture, Sports, Science and Technology of Japan; Ministry of Health, Labor and Welfare of Japan. Funding for open access charge: Innovative Cell Biology by Innovative Technology granted by the Japan Science and Technology Agency (JST).

Conflict of interest statement. None declared.

REFERENCES

1. Black,D.L. (2003) Mechanisms of alternative pre-messenger RNA splicing. *Annu. Rev. Biochem.*, **72**, 291–336.
2. Jurica,M.S. and Moore,M.J. (2003) Pre-mRNA splicing: awash in a sea of proteins. *Mol. Cell*, **12**, 5–14.
3. Reed,R. (1996) Initial splice-site recognition and pairing during pre-mRNA splicing. *Curr. Opin. Gen. Dev.*, **6**, 215–220.
4. Parker,R., Siliciano,P.G. and Guthrie,C. (1987) Recognition of the TACTAAC box during mRNA splicing in yeast involves base pairing to the U2-like snRNA. *Cell*, **49**, 229–239.
5. Gao,K., Masuda,A., Matsuura,T. and Ohno,K. (2008) Human branch point consensus sequence is yUnAy. *Nucleic Acids Res.*, **36**, 2257–2267.
6. Zorio,D.A. and Blumenthal,T. (1999) Both subunits of U2AF recognize the 3′ splice site in Caenorhabditis elegans. *Nature*, **402**, 835–838.
7. Merendino,L., Guth,S., Bilbao,D., Martinez,C. and Valcarcel,J. (1999) Inhibition of msl-2 splicing by Sex-lethal reveals interaction between U2AF35 and the 3′ splice site AG. *Nature*, **402**, 838–841.
8. Kielkopf,C.L., Rodionova,N.A., Green,M.R. and Burley,S.K. (2001) A novel peptide recognition mode revealed by the X-ray structure of a core U2AF35/U2AF65 heterodimer. *Cell*, **106**, 595–605.
9. Mullen,M.P., Smith,C.W., Patton,J.G. and Nadal-Ginard,B. (1991) Alpha-tropomyosin mutually exclusive exon selection: competition between branchpoint/polypyrimidine tracts determines default exon choice. *Genes Dev.*, **5**, 642–655.
10. Coolidge,C.J., Seely,R.J. and Patton,J.G. (1997) Functional analysis of the polypyrimidine tract in pre-mRNA splicing. *Nucleic Acids Res.*, **25**, 888–896.

11. Soares,L.M., Zanier,K., Mackereth,C., Sattler,M. and Valcarcel,J. (2006) Intron removal requires proofreading of U2AF/3′ splice site recognition by DEK. *Science*, **312**, 1961–1965.
12. Wu,S., Romfo,C.M., Nilsen,T.W. and Green,M.R. (1999) Functional recognition of the 3′ splice site AG by the splicing factor U2AF35. *Nature*, **402**, 832–835.
13. Guth,S., Martinez,C., Gaur,R.K. and Valcarcel,J. (1999) Evidence for substrate-specific requirement of the splicing factor U2AF(35) and for its function after polypyrimidine tract recognition by U2AF(65). *Mol. Cell. Biol.*, **19**, 8263–8271.
14. Guth,S., Tange,T.O., Kellenberger,E. and Valcarcel,J. (2001) Dual function for U2AF(35) in AG-dependent pre-mRNA splicing. *Mol. Cell. Biol.*, **21**, 7673–7681.
15. Pacheco,T.R., Coelho,M.B., Desterro,J.M., Mollet,I. and Carmo-Fonseca,M. (2006) In vivo requirement of the small subunit of U2AF for recognition of a weak 3′ splice site. *Mol. Cell. Biol.*, **26**, 8183–8190.
16. Vorechovsky,I. (2006) Aberrant 3′ splice sites in human disease genes: mutation pattern, nucleotide structure and comparison of computational tools that predict their utilization. *Nucleic Acids Res.*, **34**, 4630–4641.
17. Lefevre,S.H., Chauveinc,L., Stoppa-Lyonnet,D., Michon,J., Lumbroso,L., Berthet,P., Frappaz,D., Dutrillaux,B., Chevillard,S. and Malfoy,B. (2002) A T to C mutation in the polypyrimidine tract of the exon 9 splicing site of the RB1 gene responsible for low penetrance hereditary retinoblastoma. *J. Med. Genet.*, **39**, E21.
18. Faustino,N.A. and Cooper,T.A. (2003) Pre-mRNA splicing and human disease. *Genes Dev.*, **17**, 419–437.
19. Wang,X.-H., Poh-Fitzpatrick,M., Chen,T., Malavade,K., Carriero,D. and Piomelli,S. (1995) Systematic screening for RNA with skipped exons - splicing mutations of the ferrochelatase gene. *Biochim. Biophys. Acta*, **1271**, 358–362.
20. Takahashi,I., Takahashi,T., Komatsu,M., Sato,T. and Takada,G. (2002) An exonic mutation of the GH-1 gene causing familial isolated growth hormone deficiency type II. *Clin. Genet.*, **61**, 222–225.
21. Okada,K., Inoue,A., Okada,M., Murata,Y., Kakuta,S., Jigami,T., Kubo,S., Shiraishi,H., Eguchi,K., Motomura,M. *et al.* (2006) The muscle protein Dok-7 is essential for neuromuscular synaptogenesis. *Science*, **312**, 1802–1805.
22. Ikeda,Y., Takagi,A., Nakata,Y., Sera,Y., Hyoudou,S., Hamamoto,K., Nishi,Y. and Yamamoto,A. (2001) Novel compound heterozygous mutations for lipoprotein lipase deficiency. A G-to-T transversion at the first position of exon 5 causing G154V missense mutation and a 5′ splice site mutation of intron 8. *J. Lipid Res.*, **42**, 1072–1081.
23. Petroulakis,E., Cao,Z., Clarke,J.T., Mahuran,D.J., Lee,G. and Triggs-Raine,B. (1998) W474C amino acid substitution affects early processing of the alpha-subunit of beta-hexosaminidase A and is associated with subacute G(M2) gangliosidosis. *Hum. Mutat.*, **11**, 432–442.
24. Kralovicova,J. and Vorechovsky,I. (2010) Allele-specific recognition of the 3′ splice site of INS intron 1. *Hum. Genet.*, **128**, 383–400.
25. Cartegni,L., Wang,J., Zhu,Z., Zhang,M.Q. and Krainer,A.R. (2003) ESEfinder: a web resource to identify exonic splicing enhancers. *Nucleic Acids Res.*, **31**, 3568–3571.
26. Smith,P.J., Zhang,C., Wang,J., Chew,S.L., Zhang,M.Q. and Krainer,A.R. (2006) An increased specificity score matrix for the prediction of SF2/ASF-specific exonic splicing enhancers. *Hum. Mol. Genet.*, **15**, 2490–2508.
27. Fairbrother,W.G., Yeh,R.F., Sharp,P.A. and Burge,C.B. (2002) Predictive identification of exonic splicing enhancers in human genes. *Science*, **297**, 1007–1013.
28. Wang,Z., Rolish,M.E., Yeo,G., Tung,V., Mawson,M. and Burge,C.B. (2004) Systematic identification and analysis of exonic splicing silencers. *Cell*, **119**, 831–845.
29. Zhang,X.H. and Chasin,L.A. (2004) Computational definition of sequence motifs governing constitutive exon splicing. *Genes Dev.*, **18**, 1241–1250.
30. Zhang,X.H., Kangsamaksin,T., Chao,M.S., Banerjee,J.K. and Chasin,L.A. (2005) Exon inclusion is dependent on predictable exonic splicing enhancers. *Mol. Cell. Biol.*, **25**, 7323–7332.
31. Goren,A., Ram,O., Amit,M., Keren,H., Lev-Maor,G., Vig,I., Pupko,T. and Ast,G. (2006) Comparative analysis identifies exonic splicing regulatory sequences–the complex definition of enhancers and silencers. *Mol. Cell*, **22**, 769–781.
32. Sahashi,K., Masuda,A., Matsuura,T., Shinmi,J., Zhang,Z., Takeshima,Y., Matsuo,M., Sobue,G. and Ohno,K. (2007) In vitro and in silico analysis reveals an efficient algorithm to predict the splicing consequences of mutations at the 5′ splice sites. *Nucleic Acids Res.*, **35**, 5995–6003.
33. Graveley,B.R. (2001) Alternative splicing: increasing diversity in the proteomic world. *Trends Genet.*, **17**, 100–107.
34. Kosaki,A., Nelson,J. and Webster,N.J. (1998) Identification of intron and exon sequences involved in alternative splicing of insulin receptor pre-mRNA. *J. Biol. Chem.*, **273**, 10331–10337.

Biochemical and Biophysical Research Communications 411 (2011) 143–149

Contents lists available at ScienceDirect

Biochemical and Biophysical Research Communications

journal homepage: www.elsevier.com/locate/ybbrc

Molecular hydrogen inhibits lipopolysaccharide/interferon γ-induced nitric oxide production through modulation of signal transduction in macrophages

Tomohiro Itoh [a,b], Nanako Hamada [a], Riyako Terazawa [a], Mikako Ito [c], Kinji Ohno [c], Masatoshi Ichihara [d], Yoshinori Nozawa [a,e], Masafumi Ito [a,*]

[a] Department of Longevity and Aging Research, Gifu International Institute of Biotechnology, 1-1 Naka-fudogaoka, Kakamigahara, Gifu 504-0838, Japan
[b] Faculty of Agriculture, Kinki University, 3327-204 Nakamachi, Nara 631-8505, Japan
[c] Division of Neurogenetics, Center for Neurological Diseases and Cancer, Nagoya University Graduate School of Medicine, 65 Tsurumai, Showa-ku, Nagoya, Aichi 466-8550, Japan
[d] Department of Biomedical Sciences, College of Life and Health Sciences, Chubu University, 1200 Matsumoto-cho, Kasugai, Aichi 487-8501, Japan
[e] Department of Food and Health, Tokai Gakuin University, 5-68 Naka-kirinocho, Kakamigahara, Gifu 504-8511, Japan

ARTICLE INFO

Article history:
Received 7 June 2011
Available online 23 June 2011

Keywords:
Molecular hydrogen
Lipopolysaccharide/interferon γ
Macrophage
Signal transduction
Inflammatory arthritis

ABSTRACT

Molecular hydrogen has been reported to be effective for a variety of disorders and its effects have been ascribed to the reduction of oxidative stress. However, we have recently demonstrated that hydrogen inhibits type I allergy through modulating intracellular signal transduction. In the present study, we examined the hydrogen effects on lipopolysaccharide/interferon γ LPS/IFNγ-induced nitric oxide (NO) production in murine macrophage RAW264 cells. Treatment with hydrogen reduced LPS/IFNγ-induced NO release, which was associated with a diminished induction of inducible isoform of nitric oxide synthase (iNOS). Hydrogen treatment inhibited LPS/IFNγ-induced phosphorylation of apoptosis signal-regulating kinase 1 (ASK1) and its downstream signaling molecules, p38 MAP kinase and JNK, as well as IκBα, but did not affect activation of NADPH oxidase and production of reactive oxygen species (ROS). As ROS is an upstream activator of ASK1, inhibition of ASK1 by hydrogen without suppressing ROS implies that a potential target molecule of hydrogen should be located at the receptor or immediately downstream of it. These results suggested a role for molecular hydrogen as a signal modulator. Finally, oral intake of hydrogen-rich water alleviated anti-type II collagen antibody-induced arthritis in mice, a model for human rheumatoid arthritis. Taken together, our studies indicate that hydrogen inhibits its LPS/IFNγ-induced NO production through modulation of signal transduction in macrophages and ameliorates inflammatory arthritis in mice, providing the molecular basis for hydrogen effects on inflammation and a functional interaction between two gaseous signaling molecules, NO and molecular hydrogen.

1. Introduction

Accumulating evidence suggest that molecular hydrogen is effective for a number of disorders including oxidative stress-related diseases and inflammatory diseases [1]. In animal disease models, inhalation of hydrogen gas protects against cerebral infarction [2], myocardial infarction, hepatic ischemia, neonatal hypoxic brain injury, small intestine and lung transplantation, zymosan-induced inflammation, inflammatory bowel disease and sepsis. Oral intake of hydrogen-rich water exerts beneficial effects on stress-induced learning impairment, atherosclerosis, Parkinson's disease, kidney transplantation and hearing disturbance. Infusion of hydrogen-rich saline also alleviates acute pancreatitis, spinal cord injury and obstructive jaundice. In humans, oral intake of hydrogen-rich water improves lipid and glucose metabolism in patients with diabetes and impaired glucose tolerance. In most of studies, hydrogen effects have been ascribed to the reduction of oxidative stress.

We have recently demonstrated a preventive effect of oral intake of hydrogen-rich water on type I allergy in a mouse model, which is not causally associated with oxidative stress [3]. In cultured mast cells, we investigated the underlying mechanisms and found that hydrogen attenuates degranulation by inhibiting the high affinity IgE receptor (FcεRI)-mediated signal transduction but not by reducing oxidative stress. Based on these observations, we proposed that modulation of signaling pathways may be an essential mechanism underlying hydrogen effects on a broad spectrum of diseases and that hydrogen may be a gaseous signaling molecule like nitric oxide (NO).

NO is involved in a variety of important physiological processes such as vasodilatation, neurotransmission and host defense against

* Corresponding author. Fax: +81 58 371 4412.
E-mail address: mito@giib.or.jp (M. Ito).

0006-291X/$ - see front matter © 2011 Elsevier Inc. All rights reserved.
doi:10.1016/j.bbrc.2011.06.116

invading pathogens [4]. However, an excessive amount of NO is detrimental, resulting in rheumatoid arthritis, gastritis, bowel inflammation and bronchitis [5,6]. In macrophages, NO is synthesized by inducible isoform of nitric oxide synthase (iNOS), which catalyzes the reaction of L-arginine to L-citrulline and NO, in response to various stimuli such as lipopolysaccharide (LPS), interferon (IFN), tumor necrosis factor α (TNFα) and interleukin 1β (IL1β) [7]. LPS binds to the cell surface receptor CD14, which triggers activation of toll like receptor 4 (TLR4) and the downstream signaling molecules such as IκB and mitogen-activated protein kinases (MAPKs) including c-Jun NH_2-terminal protein kinase (JNK), p38 MAP kinase and extracellular signal-regulated kinase (ERK) [8]. TLR4 signaling activates transcription factors such as nuclear factor kappa B (NFκB), activator protein 1 (AP1) and ELK1, culminating in the expression of pro-inflammatory genes including iNOS, cyclooxygenase 2 (COX2), TNFα and IFNβ. On the other hand, IFNβ and INFγ, respectively, bind to type I and type II IFN receptors expressed on the surface of macrophages, and activate Janus kinase (JAK)–signal transducers and activators of transcription (STAT) signaling, resulting in up-regulation of IFN regulatory factor 1 (IRF1) [9]. Both IRF1 and STAT1 bind to the iNOS promoter and enhance production of NO.

Previous reports have demonstrated that hydrogen treatment attenuates inflammation in animal models of inflammatory diseases such as zymosan-induced inflammation [10] and inflammatory bowel disease [11], but the underlying molecular mechanisms are not yet understood. According to our recent findings [3], we hypothesized that hydrogen might modulate the inflammatory signal transduction and that there might be a functional interaction between two gaseous signaling molecules, NO and molecular hydrogen. In the present study, we examined the effects of hydrogen on LPS/IFNγ-induced signal transduction and NO production in murine RAW264 macrophage cells. We also studied the hydrogen effects on anti-type II collagen antibody-induced arthritis in mice, a model for human rheumatoid arthritis.

2. Materials and methods

2.1. Antibodies

The antibodies to p-ASK1 (Ser967/Thr845), AKT, p-AKT, p44/42 MAP kinase (ERK1/2), p-p44/42 MAP kinase (Thr202/204), SAPK/JNK, p-SAPK/JNK (Thr180/Tyr204), p38 MAP kinase, p-p38 MAP kinase (Thr180/Tyr182), iNOS, COX2 TAK1, p-TAK1 (Ser412/Thr184/187), IκBα, p-IκBα (Ser32/36), NFκB p65, STAT1α and p-STAT1α (Tyr701) were purchased from Cell Signaling Technology (Beverly, CA, USA). The antibodies against $p22^{phox}$, $p47^{phox}$, $p67^{phox}$ and $gp91^{phox}$ were from Santa Cruz Biotechnology (Santa Cruz, CA, USA). Anti-ASK1, -histone H3 and -β-actin antibodies were obtained from Abcam (Cambridge, MA, USA), Upstate (Lake Placid, NY, USA) and Sigma–Aldrich (St. Louis, MO, USA), respectively.

2.2. Cell culture and hydrogen treatment

Murine macrophage RAW264 cells were purchased from RIKEN BioResource Center (Tsukuba, Japan) and cultured in Dulbecco's modified Eagle's medium (DMEM) containing 10% heat-inactivated fetal bovine serum (FBS), 100 U/ml of penicillin and 100 μg/ml streptomycin in a humidified atmosphere of 5% CO_2 at 37 °C. Hydrogen treatment was performed as described previously with a slight modification [3]. Briefly, cells seeded onto multi-well plates were incubated at 37 °C under a humidified condition of 75% H_2, 20% O_2 and 5% CO_2, or 95% air and 5% CO_2 in a small aluminum bag. After 24 h incubation in the presence of hydrogen, the hydrogen concentration in the culture media was about 0.3 ppm as measured by using the H_2–N hydrogen needle sensor (Unisense, Aarhus, Denmark). After treatment with or without hydrogen for 24 h, cells were treated with or without LPS (final concentration, 200 ng/ml) (Sigma–Aldrich) and IFNγ (final concentration, 25 ng/ml) (Millipore, Bedford, MA, USA), which was followed by incubation in the presence or absence of hydrogen.

2.3. Measurement of nitric oxide production

Cell culture media were centrifuged at 4 °C for 5 min and the supernatant was subjected to measurement of the amount of nitrite, a stable metabolite of NO, using the Griess reagent kit (Promega, Madison, WI, USA).

2.4. Western blot analysis

Whole cell extracts were prepared by lysing in RIPA buffer containing the complete protease inhibitor cocktail and the phosphatase inhibitor cocktail (Roche, Penzberg, Germany). The cytosolic and nuclear fractions were separated by the NE-PER nuclear and cytoplasmic extraction kit (Thermo Fisher Scientific, Waltham, MA, USA). The cytosolic and membrane fractions were isolated using the ProteoExtract subcellular proteome extraction kit (Merk KGaA, Darmstdt, Germany). Samples were subjected to sodium dodecyl sulfate–polyacrylamide gel electrophoresis (SDS–PAGE) and electroblotted onto PVDF membranes. Membranes were incubated with a primary antibody, followed by incubation with a horseradish peroxidase-conjugated secondary antibody. Immunolabeled proteins were detected using the ECL chemiluminescence kit (GE Healthcare, Piscataway, NJ, USA) and the LAS-4000 lumino-image analyzer (Fujifilm, Tokyo, Japan).

2.5. Quantitative RT-PCR

Total RNA was extracted from cells by the TRIzol reagent (Invitrogen, Carlsbad, CA, USA) followed by DNase I treatment. cDNA was synthesized using the PrimeScript reagent kit (Takara Bio, Ohtsu, Japan) and subjected to quantitative RT-PCR using the Thermal Cycler Dice real-time PCR system (TP800, Takara Bio). Primers for *iNOS* and *GAPDH* were purchased from Takara Bio. The expression level of *iNOS* gene was determined using the comparative C_t method and normalized to that of *GAPDH*. The PCR consisted of 45 cycles (95 °C for 10 s, 60 °C for 40 s and 72 °C for 1 s) after an initial denaturation step (95 °C for 10 min).

2.6. Measurement of intracellular ROS levels

Intracellular levels of reactive oxygen species (ROS) were determined using a cell-permeable fluorescent probe, CM-H_2DCF-DA (Invitrogen). Cells were incubated with 10 μM CM-H_2DCF-DA for 1 h at 37 °C. After treatment, cells were washed twice with PBS and lysed in RIPA buffer. The absorbance of the lysates was measured with excitation at 490 nm and emission at 530 nm using the MTP-600 fluorometric imaging plate reader (Corona Electric, Ibaraki, Japan).

2.7. Hydrogen treatment of mice

Five-weeks-old female BALB/c Cr Slc mice (Japan SLC, Hamamatsu, Japan) were fed with either hydrogen-rich or control water *ad libitum*, as described previously [3]. Hydrogen-rich water packed in aluminum pouches was purchased from Blue Mercury (Tokyo, Japan). The hydrogen concentration of the hydrogen-rich water was approximately 1.0 ppm. The control water was prepared by gently stirring the hydrogen-rich water in open air for 24 h. This study was approved by the Animal Use Committee of the Gifu